RADAR IMAGING GLACIO-VOLCANIC STRATIGRAPHY: MT. WRANGELL, ALASKA

by

GUY MATTHEW CROSS

B.A.(Geophysics), The State University of New York, 1982

A THESIS SUBMITTED IN PARTIAL FULFILLMENT OF

THE REQUIREMENTS FOR THE DEGREE OF

MASTER OF SCIENCE

in

THE FACULTY OF GRADUATE STUDIES

Department of Geophysics and Astronomy

We accept this thesis as conforming

to the required standard

THE UNIVERSITY OF BRITISH COLUMBIA

April 1987

In presenting this thesis in partial fulfilment of the requirements for an advanced degree at the University of British Columbia, I agree that the Library shall make it freely available for reference and study. I further agree that permission for extensive copying of this thesis for scholarly purposes may be granted by the head of my department or by his or her representatives. It is understood that copying or publication of this thesis for financial gain shall not be allowed without my written permission.

Department of Geophysics and Astronomy

The University of British Columbia
1956 Main Mall
Vancouver, Canada
V6T 1Y3

Date February 24, 1987

ABSTRACT

An airborne radar survey was conducted over the ice-filled volcanic caldera at Mt. Wrangell, Alaska. Research reported here involves computer processing and interpretation of radio-reflection data acquired over 21 traverses of the summit. In addition to describing useful data enhancement techniques, a dynamic programming approach is introduced for topographically controlled data positioning and spatial correction. Interpretation focusses upon a well defined radio-stratigraphy attributed to high acidity horizons deposited at the ice surface during periods of elevated volcanic activity. A comparative analysis of layer character indicates that echoes from the caldera floor are not continuously detected because of anomalously high signal absorption. Consequently, results impose a lower limit upon maximum ice thickness. A numerical interpretation scheme, incorporating both glaciological measurements and empirical relations governing the behaviour of firn and ice, is developed to aid interpretation of the glacio-volcanic stratigraphy. Preliminary modelling yields a speculative volcanic record that roughly matches the known eruption sequence at Mt. Wrangell and suggests a significant extension of the volcanic history.

With great
admiration
for
my parents.

TABLE OF CONTENTS

LIST OF TABLES

LIST OF FIGURES

ACKNOWLEDGEMENTS

First and foremost, I am grateful to my supervisor, G.K.C. Clarke. His thoughtful guidance and enduring patience are most appreciated. I also thank C.S. Benson of the Geophysical Institute, University of Alaska, and B.T. Prager, B.B. Narod and W.S.P. Leaney of UBC for fruitful discussions and advice. Finally, I express my appreciation to the entire faculty, staff and graduate student body of the Department of Geophysics and Astronomy, UBC, for providing an interesting and pleasant environment.

Research has been funded by the National Sciences and Engineering Research Council of Canada.

CHAPTER I

INTRODUCTION

1.1 Mt. Wrangell

The Wrangell Mountains are located in the south-eastern interior of Alaska and roughly parallel the coastal Chugach range (Figure 1.1). Both ranges are westward-extending branches of the St. Elias Mountains, which are located in the south-western extreme of the Yukon Territory. Owing to their geographical location and high elevation, the Wrangell Mountains receive abundant snowfall that maintains thorough glaciation of the range. Despite an icy outward appearance, the Wrangell mountains constitute an active link in the circum-Pacific chain of andesitic volcanism. Mt. Wrangell, itself, is a broad shield volcano, the summit of which rises 4317 m (14,163 ft) above sea-level. The summit is characterized by a geologically recent collapse caldera, with three post-calderan craters situated along the northern rim (Figures 1.2 and 1.3). Although recent volcanic activity has mainly occurred within the marginal craters, high geothermal heat flux is also expected at the caldera floor. Nonetheless, glacier ice completely fills the roughly 4 $\times$ 6 km oblong caldera and overflows into Long Glacier at a breach in the southern rim. In addition to posing a significant flood hazard, this unique situation provides an ideal opportunity to study glacier-volcano interaction.

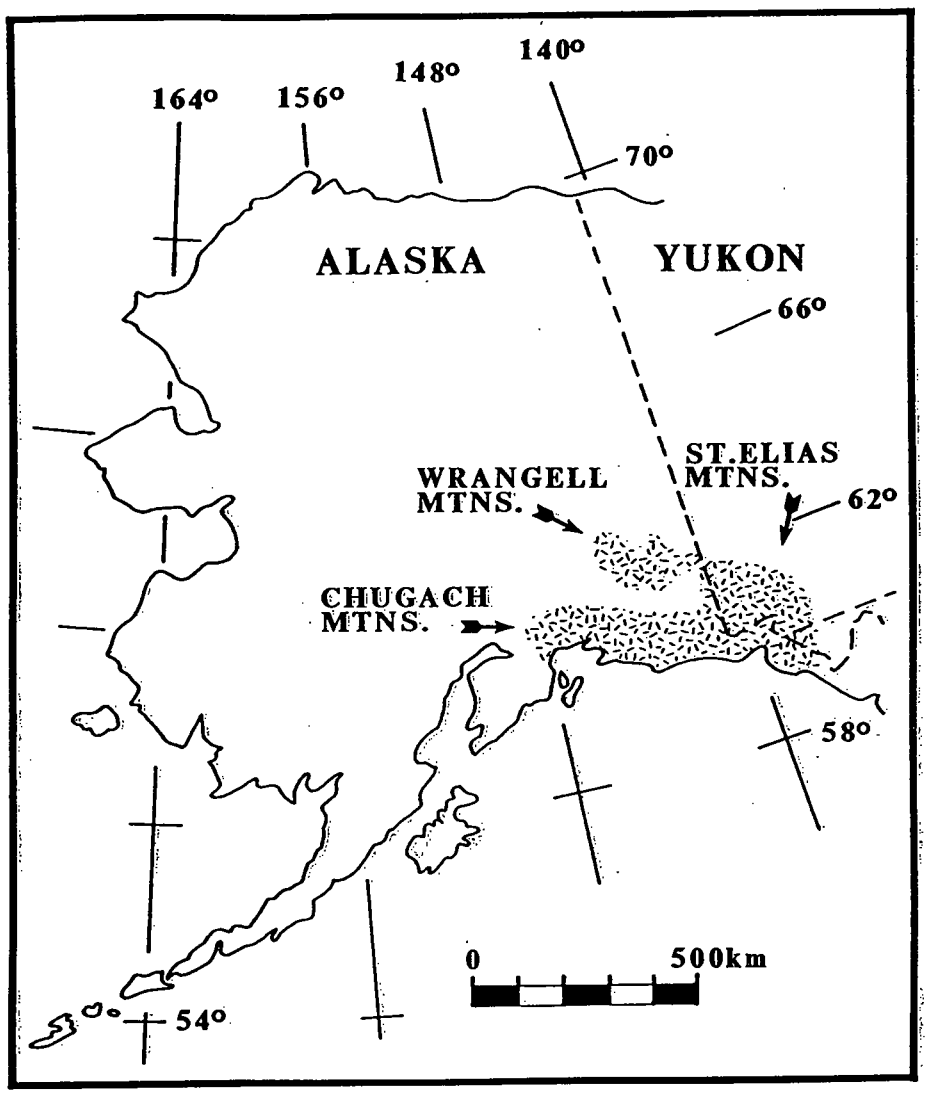

Figure 1.1. Project location, depicting the Wrangell Mountains in relation to associated ranges.

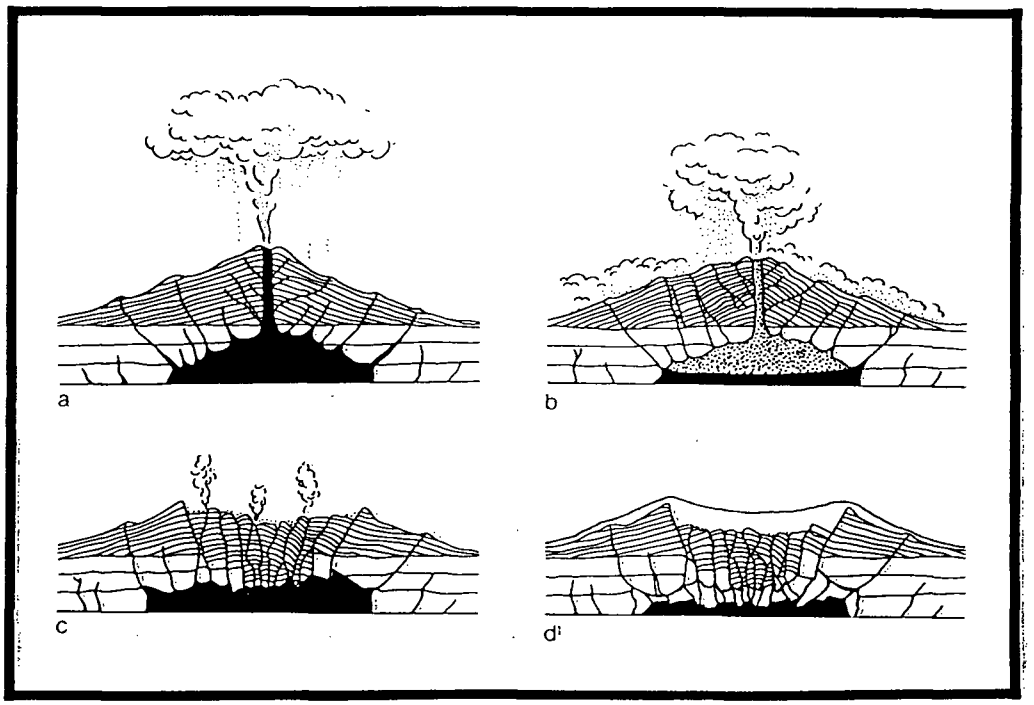

Figure 1.2. Postulated evolution of the summit caldera at Mt. Wrangell. (a and b) Eruptions from the pre-calderan summit deplete the magma chamber below. (c) Formation of the caldera by collapse into depleted magma chamber. (d) Cooling and further subsidence of the magma chamber give rise to the present ice mantled condition (adapted from Press and Siever, 1974).

1.2 Glacier-Volcano Interaction

Researchers from the Geophysical Institute of the University of Alaska measured surface elevation within the summit caldera in 1965, 1975, 1976 and 1978. With the exception of sites in close proximity to the anomalously active North Crater, the elevation was found to remain constant, within 1 m, over the 13 year period (Bingham, 1967; Motyka, 1983). In addition, a mean surface temperature of -21 ^{o}C was reported with a suggestion that seasonal melting at the surface is negligible. On the basis of these observations, Benson and Motyka (1978) concluded that net annual ice-equivalent accumulation at the surface of the caldera is roughly balanced by a

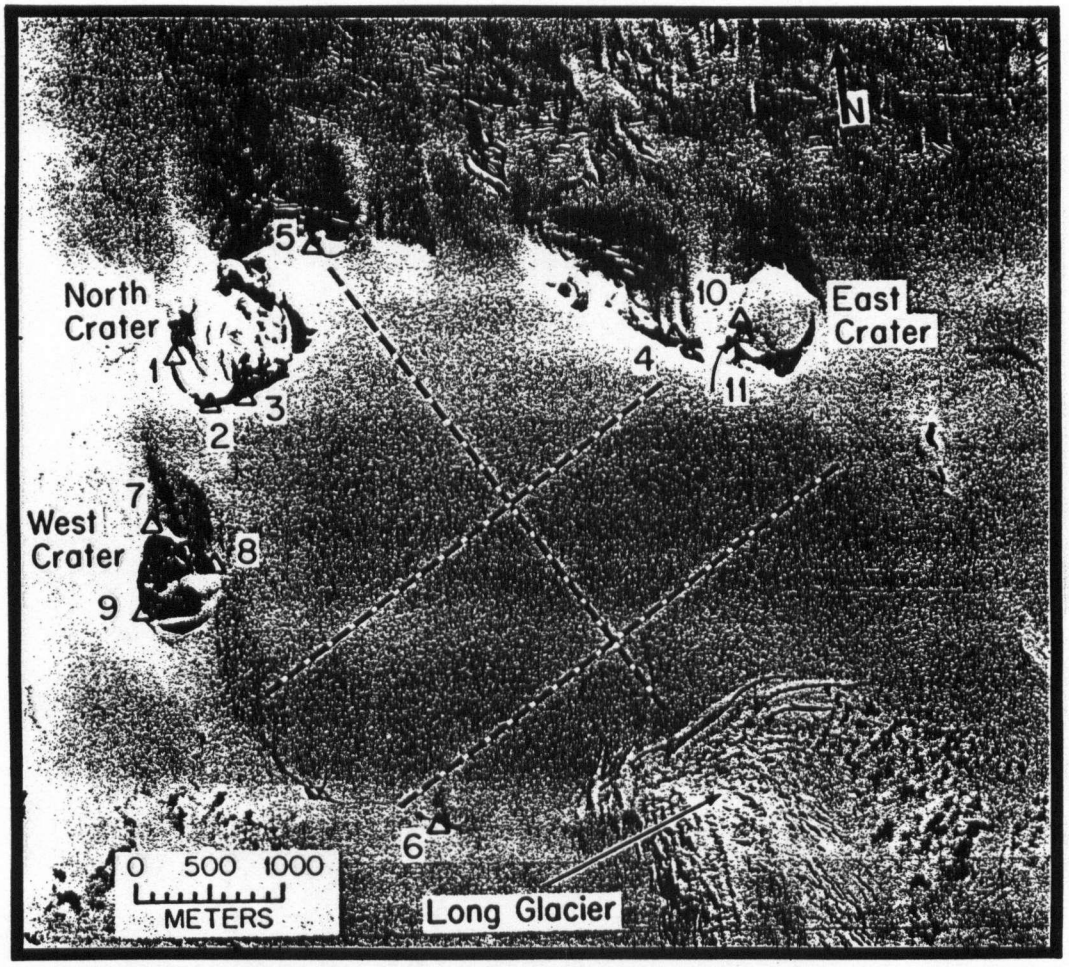

Figure 1.3. 1975 photograph of the summit caldera, denoting the location of the three post-calderan craters and Long Glacier. Numbers identify survey control features. Dashed lines indicate survey lines.

combination of geothermally fuelled basal melting and outflux of ice via Long Glacier. The approximate conservation of ice-equivalent precipitation to and from the caldera glacier maintains the surface in a quasi steady-state condition and has prompted a "giant calorimeter" analogy. By determining the ice-equivalent surface accumulation rate and an approximate ice flux at the head of Long Glacier, a rough estimate of the overall basal melt rate can be obtained. Assuming that the present accumulation rate

has persisted for the last 2000 years, Benson and Motyka (1978) estimated an upper limit of 140 HFU (5.88 W/m^2) on the equilibrium heat flux at the caldera floor. More precise estimates require detailed knowledge of ice thickness and flow velocity within the caldera, especially in the vicinity of Long Glacier.

1.3 Radioglaciology

A programme of ground-based radar probing experiments was initiated by the Geophysical Institute in 1976 (Benson, 1982). In addition to detecting internal reflections from within the ice mass, localized echo-soundings suggested a maximum ice thickness approaching 900 m in the central region of the caldera. Detection of internal layer echoes indicated the existence of a well-preserved glacio-volcanic stratigraphy, and supported a proposed ice-coring project that would furnish a combined record of climatic variation and volcanic activity. In April of 1982, the UBC 840 MHz ice radar system was employed along 21 airborne traverses of the caldera (Figure 1.4). The reconnaissance was intended to guide the selection of core drilling sites and provide continuous caldera geometry profiles for confirmation of previous echo-soundings. Although reflections from the glacier bed were restricted by anomalously high signal absorption rates, a well defined radio- stratigraphy was recorded, and is attributed to high-acidity horizons deposited at the ice surface during periods of elevated volcanic activity. Prior to presenting interpretive results, however, the data processing phase of the project is described, including signal enhancement techniques and a computer-based method for positioning airborne data.

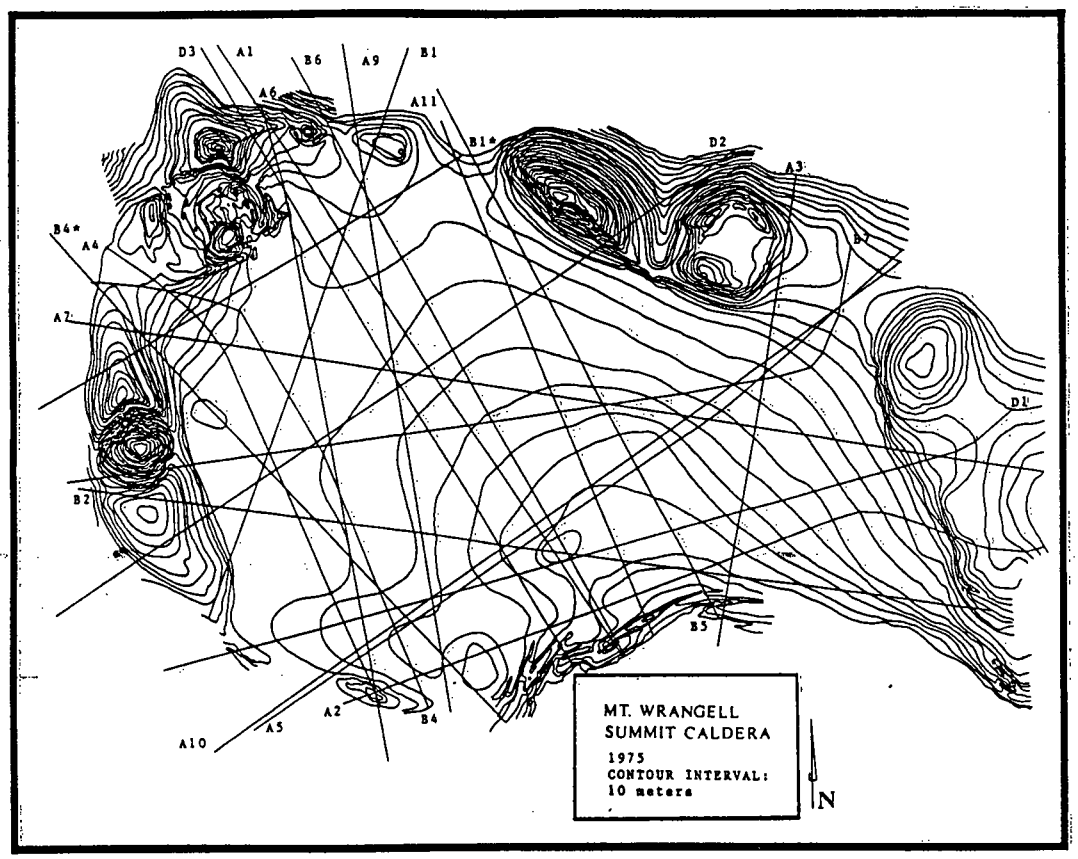

Figure 1.4. Flight-line map. Flight-line designation is indicated at the head of each traverse.

CHAPTER II

DATA ACQUISITION AND PROCESSING

2.1 Data Acquisition

The UBC radio-echo sounder (Narod and Clarke, 1980; 1983) operates at a centre frequency of 840 MHz. A bandwidth of 40 MHz requires a Nyquist sampling frequency of 80 MHz which, in turn, implies a sampling interval of 12.5 ns. To avoid the required sampling rate, the UBC system is designed for data acquisition based upon a strobing technique. Rather than sample a single returned waveform at the necessary rate, we acquire a 1024-point data trace over 1024 consecutive returns. A sampling time base incrementally adjusts the acquisition time and generates a trigger pulse for the transmitter. A pulse repetition rate of 10 kHz provides an effective sampling interval of 10 ns. Although small-scale variations are produced by interference effects, the average structure of the waveform is assumed to remain consistent over the 1024 returns required to acquire a sampled version. Practical considerations support this assumption. The system antenna is characterized by an E-plane beam width of 18^o (3 dB down) parallel to flight heading. At a ground clearance of 200 m, the radar illuminates a surface region with a dimension of approximately 60 m along the flight-track. In comparison, at a ground speed of 60 m/s (roughly 120 mi/hr), the aircraft proceeds approximately 6 m along the traverse during the roughly 100 ms required to fully sample the returned waveform. Clearly, the data redundancy is more than sufficient to justify the strobing assumption.

2.2 Data Enhancement

2.2.1 Background

Historically, radioglaciological data have been recorded photographically. The returned waveform is displayed for recording purposes on an oscilloscope in either A-scope or Z-scope formats. Although the Z-scope format can be used to generate intensity-modulated time sections for interpretation, photographic recording restricts the application of post-acquisition enhancement and display techniques. The UBC system output, on the other hand, is recorded on analogue magnetic tape and subsequently input to an analogue/digital converter. The resulting digital data format allows the use of seismic data enhancement techniques (Sherrif and Geldart, 1983; Prager, 1983).

A simple and effective enhancement scheme is employed to improve the signal to noise (S/N) ratio. Elements of this scheme include median-based filtering techniques and lateral trace averaging (stacking). Median filters are particularly well suited for removal of spurious noise from signals that are characteristically monotonic over n-length segments or constant over a duration of $(n+1)/2$ samples (Evans, 1982; Nodes and Gallagher, 1982). A combination of power fading in the returned signal and receiver design causes typical ice-sounding radar data to possess such a character. For this reason, median-based filters are given a prominent role in the applied enhancement scheme. Subsequent sections describe individual procedures in order of application.

2.2.2 Median Residual Filtering

The power envelope of a radio-echo is typically characterized by a sharp onset to maximum amplitude. Subsequently, the power decays monotonically at a fading rate controlled by surface roughness. Relatively low amplitude reflection events are commonly superimposed upon the fading tail of major echoes, especially upon the surface reflection. Median residual filtering removes gross structure caused by large scale-fading and emphasizes less apparent echoes. The task is accomplished by subtracting a median filtered version from the raw data trace. Although for practical purposes the median removes low frequency trends, the residual is not strictly a "high passed" result. Unlike the moving average, which effectively smoothes sharp signal variations, the running median filter (RMF) is non-linear and preserves straight-edged step features while events of relatively short duration are suppressed. As a result, the median residual is characterized by less pronounced side lobes and greater resolution of small scale events (Figure 2.1).

Residual filtering is a preparatory procedure for subsequent median despiking (Section 2.2.4). Claerbout and Muir (1973) suggested that the desired RMF window length may require compensation for effective contraction due to regional signal gradients. Removal of gross structure by residual filtering allows subsequent application of an optimum median despiker.

2.2.3 Average Stacking

Average stacking (Robinson, 1970; Prager, 1983) replaces each data trace by a spatially-averaged version estimated over n adjacent traces. The stacked trace is

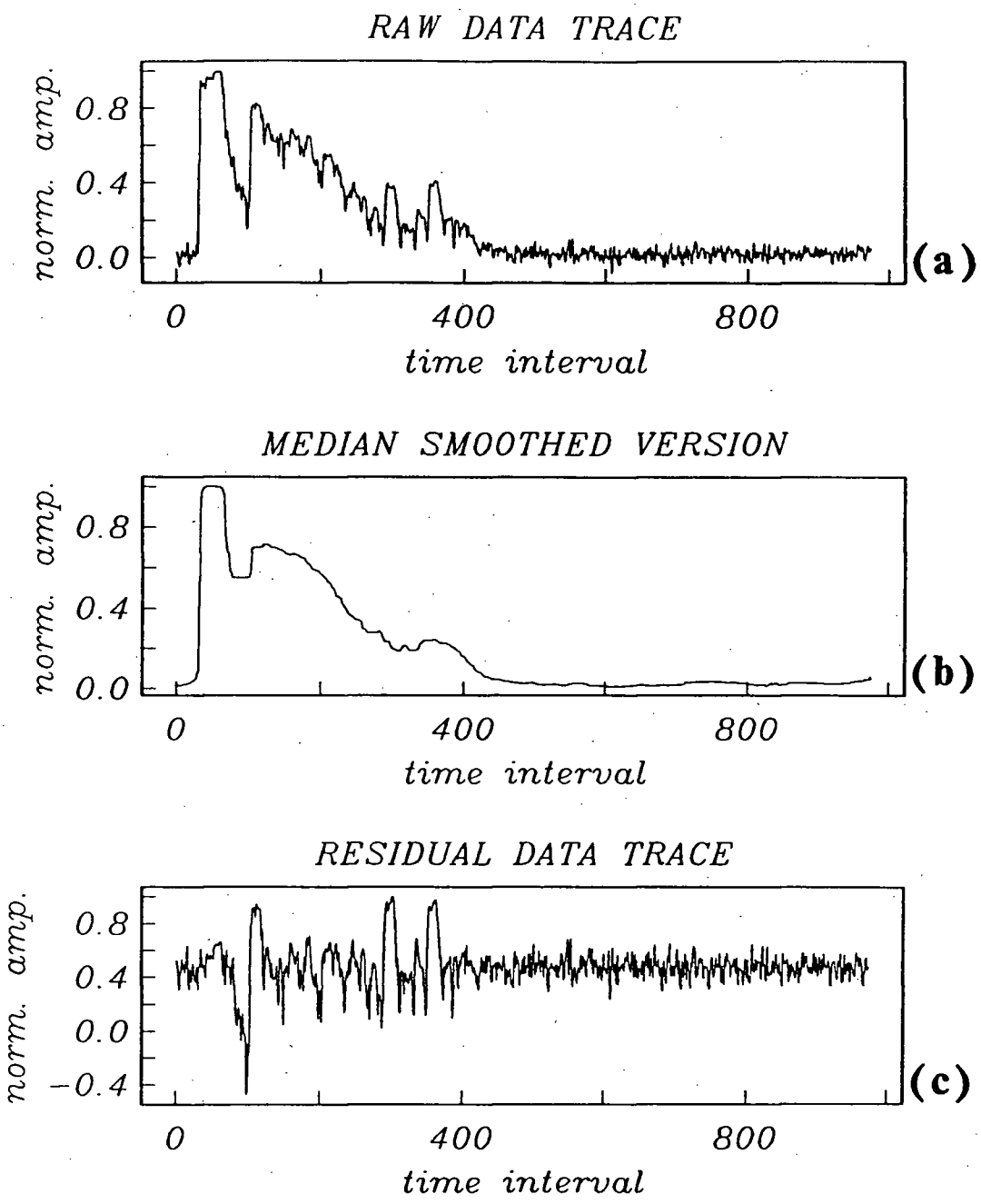

Figure 2.1. Median residual filtering. (a) Raw data trace. (b) Smoothed data trace obtained by application of a 51-point running median filter. (c) Residual data trace formed by subtracting broad scale structure from the raw data trace.

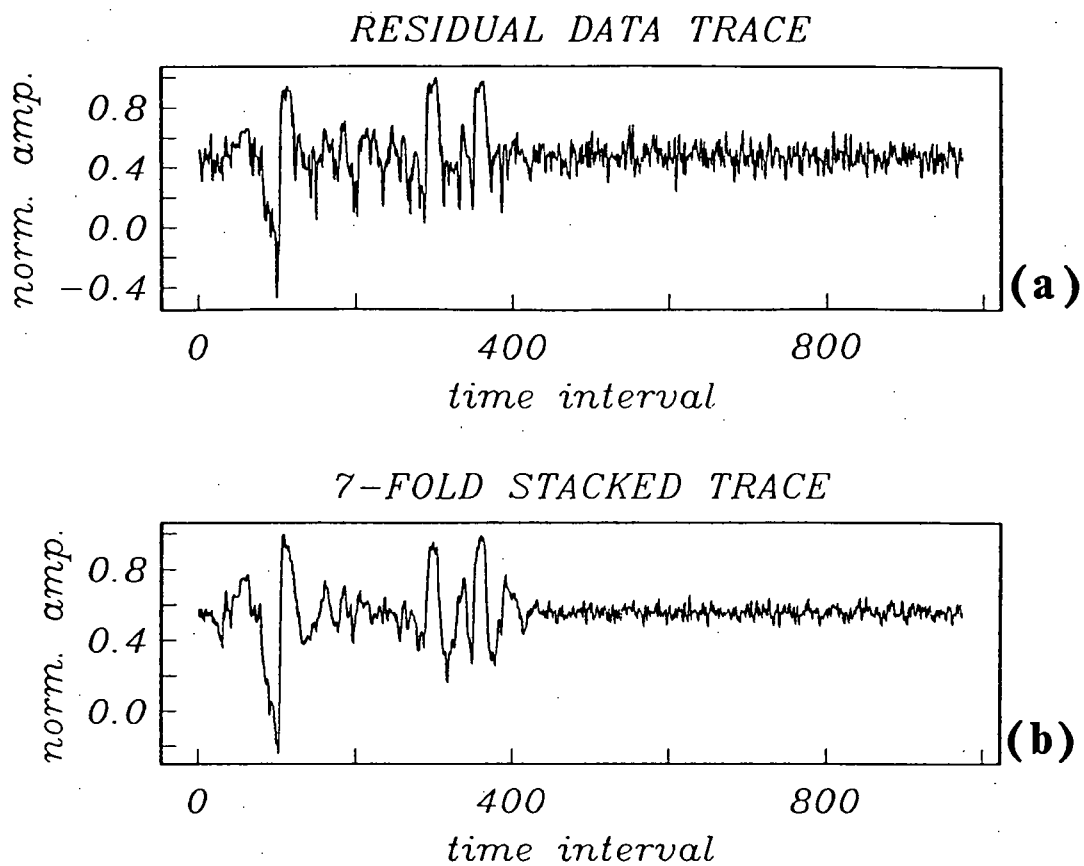

Figure 2.2. Average stacking. (a) Median residual data trace (see previous figure). (b) Average stacked trace formed at the midpoint of a 7-trace window.

formed at the midpoint of the n-length window. An underlying assumption for optimum stacking requires that the n adjacent traces be identical except for additive noise. For purely random noise, an n-fold average stack improves the S/N ratio by a factor of $\sqrt{n}$. In Section 2.1 it was demonstrated that a ground clearance of 200 m and a ground speed of 60 m/s results in roughly 10-fold data redundancy. Nonetheless, the stack fold must be selected with regard for a trade-off between S/N ratio and smearing of coherent energy. A conservative 7-fold stack is applied in the present scheme (Figure 2.2).

2.2.4 Median Despiking

Median residual filtering (Section 2.2.2) attempts to retain only gross structure in initial filtering, so that events of shorter duration are emphasized in the residual trace. While enhancing desirable features, however, the method also preserves spurious noise impulses. Although stacking reduces random noise appreciably, a running median despiker is applied to further improve the S/N ratio. Application of an n-length RMF preserves features with duration exceeding approximately $(n-1)/2$ samples. Events of shorter duration are suppressed. In comparison to the median residual filter, the median despiker operates over a relatively brief window defined by the duration of the shortest non-noise event. According to Evans (1982), the optimum RMF window length is given by

$$n = 2(m/s - 3/2), \tag{2.1}$$

where m represents the duration of the shortest non-noise event and s is the sampling interval. The UBC system is characterized by a sounding pulse duration of 50 ns, including a rise time of 18 ns and a fall time of 28 ns. The effective sampling interval is 10 ns. Assuming that the minimum non-noise event duration is roughly equivalent to the total pulse duration, we obtain an optimum RMF window length of 7 samples (Figure 2.3).

2.2.5 Conclusion

The cumulative effect of data enhancement procedures is illustrated by Figure 2.4. The simple methods described above yield impressive enhancement of the raw data. Median-based filtering techniques have proved to be well suited for enhancement of

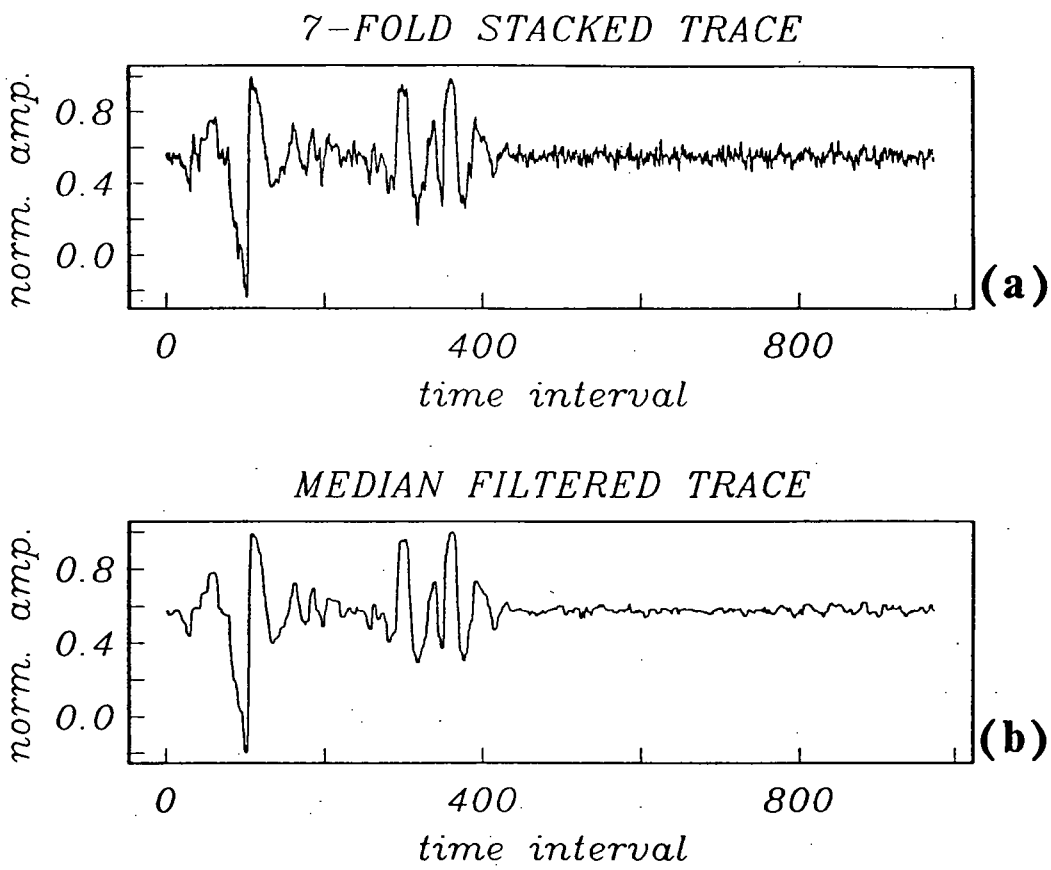

Figure 2.3. Median despiking. (a) 7-fold stacked residual trace (see previous figure). (b) Filtered trace obtained by application of a 7-point median despiker.

ice-sounding radar data and should find future application in radioglaciology. Possible improvements upon these techniques might include non-uniform weighting (Claerbout and Muir, 1973) and iterative filter application (Fitch and others, 1985).

2.3 Data Positioning and Spatial Correction

2.3.1 Introduction

Sound deductions concerning reflector geometry and ice dynamics require spatially accurate data. Although airborne traverses are controlled by maintaining a constant flight-heading between obvious topographic features, regional and local variations in

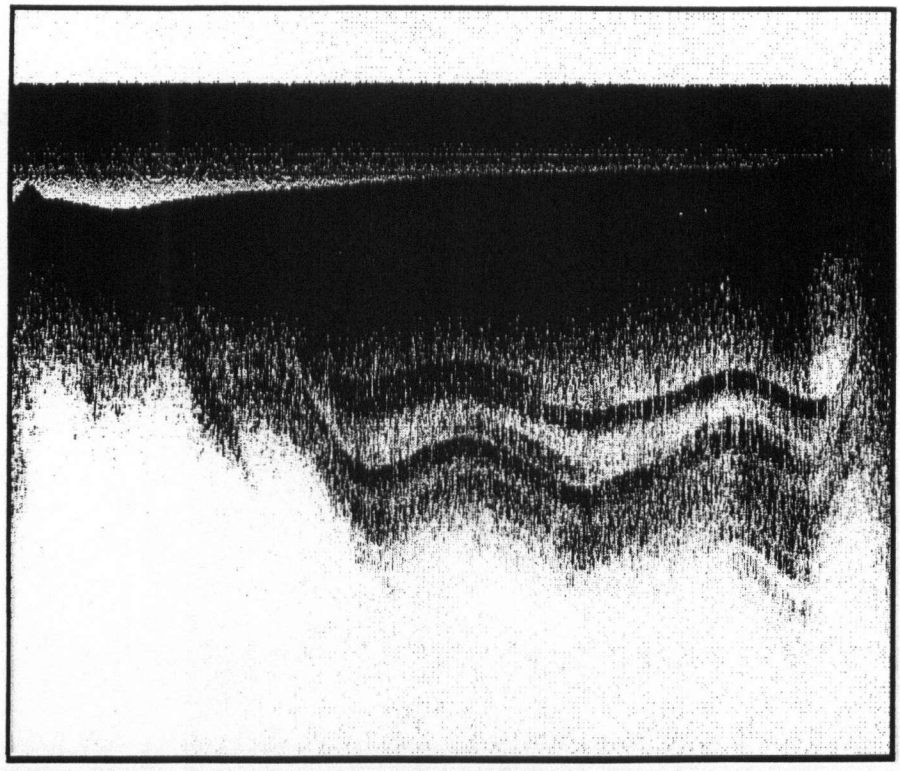

(a)

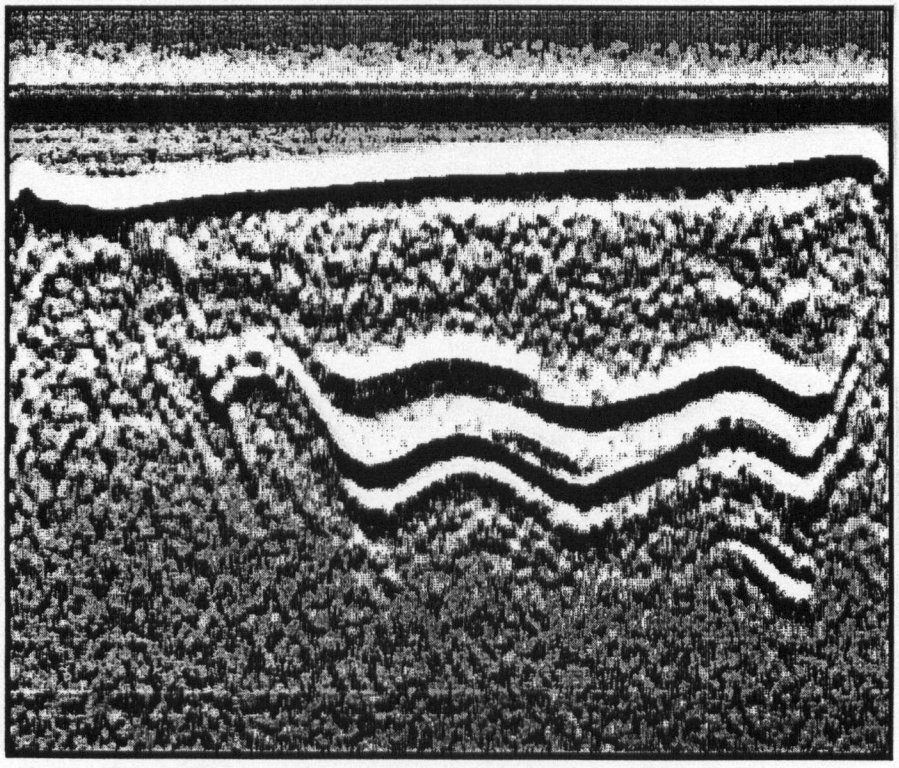

(b)

Figure 2.4. Cummulative enhancement effect. (a) Raw time section. (b) Equivalent time section after enhancement processing. Figures 2.1 - 2.3 illustrate the sequence of processing steps leading from the raw time section (a) to the enhanced result (b).

altitude and ground speed produce spatial distortions in the recorded data. Consequently, the surface reflection profile is a spatially distorted record of terrain relief along the traverse. By constraining the distorted profile to match the actual topography, spatial sampling errors are compensated and individual data traces are approximately located in northing, easting and elevation coordinates. A computational procedure for profile alignment is described and illustrated below.

2.3.2 Flight Trajectory and Vertical Distortion

The alignment procedure begins with preparation of reference (topographic) and data (surface reflection) profiles. The reference profile is obtained directly from the topographic base map. Assuming accurate orientation of the traverse line, intersections of the flight-track with topographic contours are digitized, providing an elevation profile constrained in northing and easting coordinates (Figure 2.5). A tensioned cubic spline is fit to the resulting profile and resampled at equal intervals. The sampling interval is adjusted so that the reference topographic profile and the surface reflection profile are of equal length. The surface reflection profile is obtained as the inverse profile of first arrival time along the traverse (Figure 2.6). A moving average operator is applied to reduce receiver chatter over the resulting profile.

If altitude and ground speed remain constant over the traverse, reference and data profiles should be identical. Comparison of the resulting profiles establishes the existence of pronounced spatial distortions in the data profile. Most notably, the regional relief gradient is reversed. This effect is explained in terms of the gross flight trajectory. Since the surface reflection profile represents a continuous record of sounding range, a simple linear flight trajectory, departing from constant altitude,

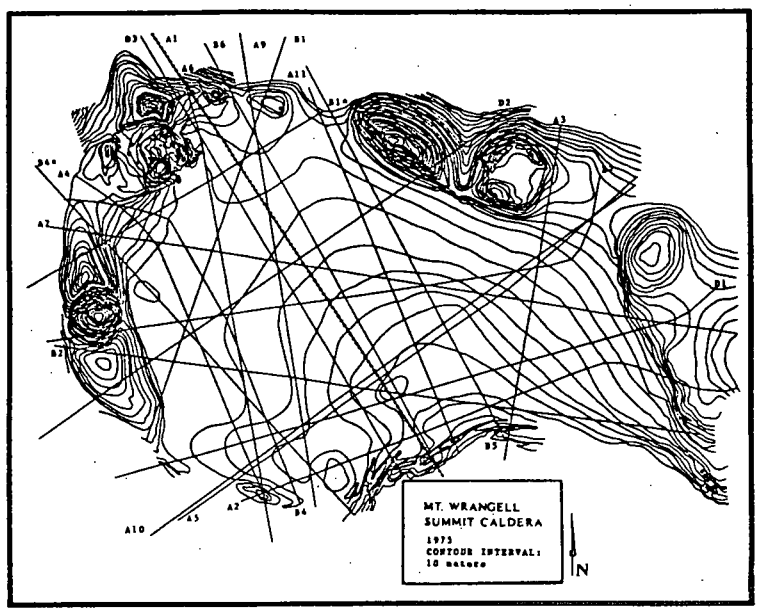

(a)

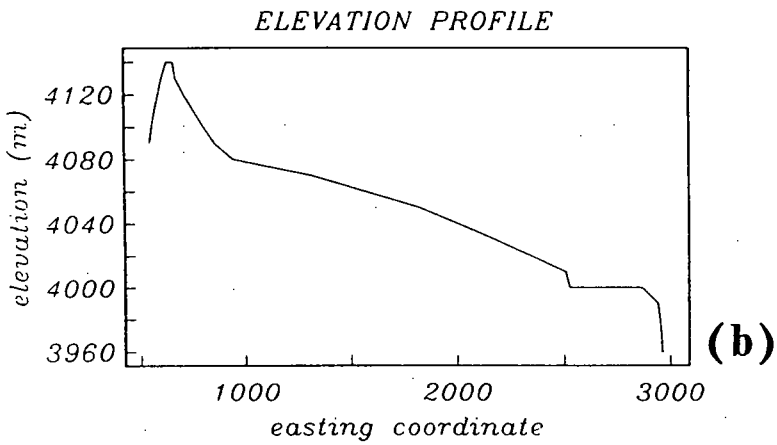

(b)

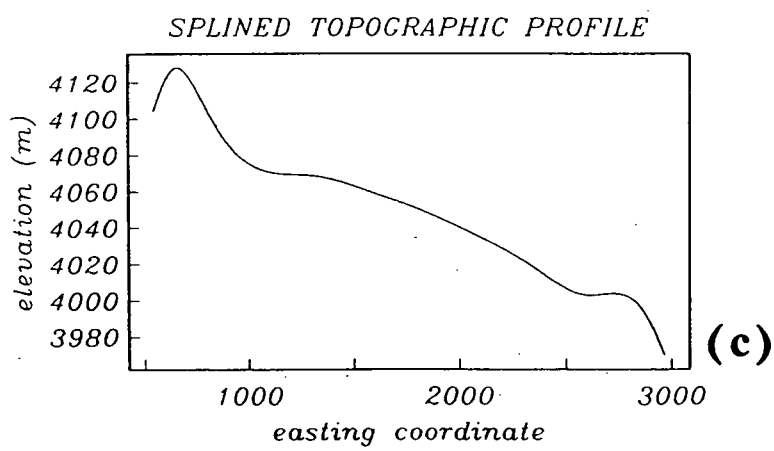

(c)

Figure 2.5. Formation of the reference topographic profile. (a) Intersections between traverse line A1 (dotted) and topographic contours are located in horizontal coordinates. (b) Traverse line-contour intersections form the basic elevation profile. (c) Tensioned cubic spline interpolation produces a naturally smoothed profile.

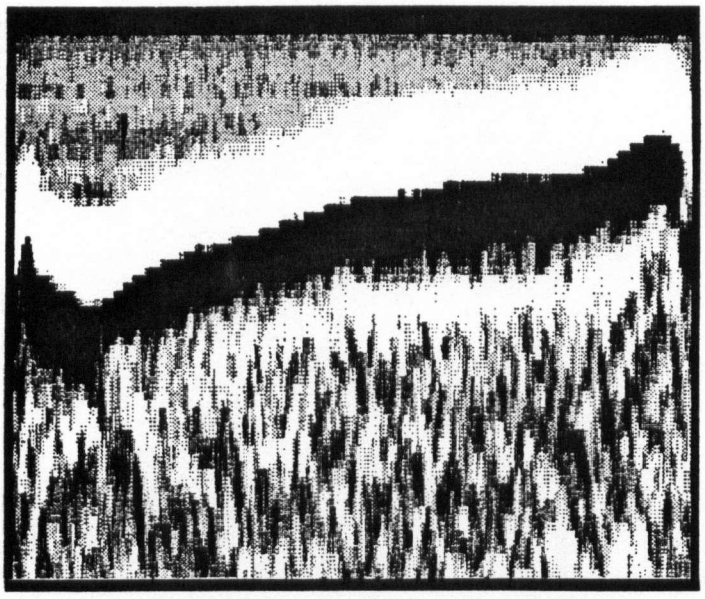

(a)

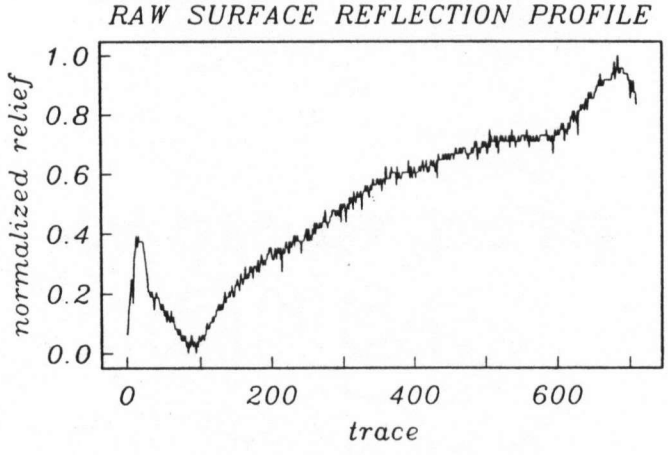

(b)

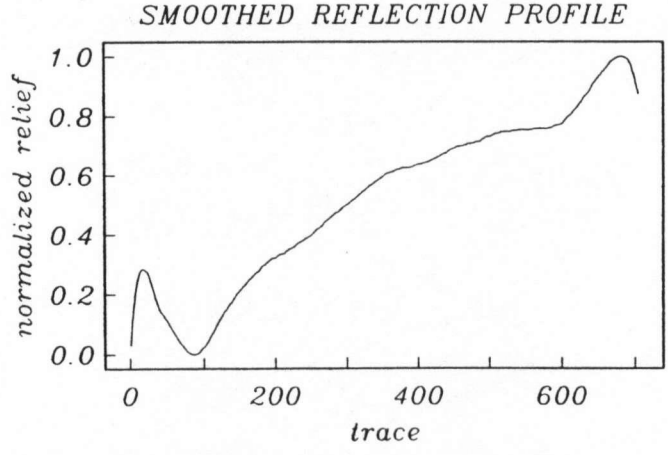

(c)

Figure 2.6. Formation of the data relief profile. (a) Time section depicting raw surface reflection. (b) Surface reflection profile obtained directly as the inverse profile of first arrival time. (c) Application of moving average operator produces smoothed relief profile.

is capable of producing the observed trend reversal. Although the actual trajectory is likely more complex, the regional gradient is removed from both reference and data profiles as a first approximation (Figure 2.7). The resulting residual data profile retains second-order vertical distortions caused by local altitude variations. These local fluctuations are compensated to a large extent by piece-wise linear amplitude rescaling between obvious control features that are mutually apparent in the residual profiles (Figure 2.8). Large-scale topographic extrema serve as control features; in the case of Mt. Wrangell: the caldera rim and central crest.

At this stage, remaining dissimilarities between the residual profiles are assumed to result from regional and localized ground speed variations.

2.3.3 Ground Speed Variation and Lateral Distortion

Deviations from constant ground speed result in relative compressions and/or extensions of the data profile. These lateral distortions are corrected by exploiting a dynamic programming approach to waveform alignment (Myers and Rabiner, 1981; Anderson and Gaby, 1983). The vertical rescaling procedure, described in the previous section, effectively involves the application of a user supplied matching function in vertical profile coordinates. Dynamic waveform alignment determines a completely analogous warping function in horizontal coordinates by means of a two-stage procedure.

The initial stage of the waveform alignment procedure involves a statistical comparison of the vertically corrected residual profiles. A coherency map is generated by calculating a normalized coherency measure, $S(r,d)$, over a two-dimensional grid. $S(r,d)$ is formed by computing the semblance (Neidell and Taner, 1971) over l-length

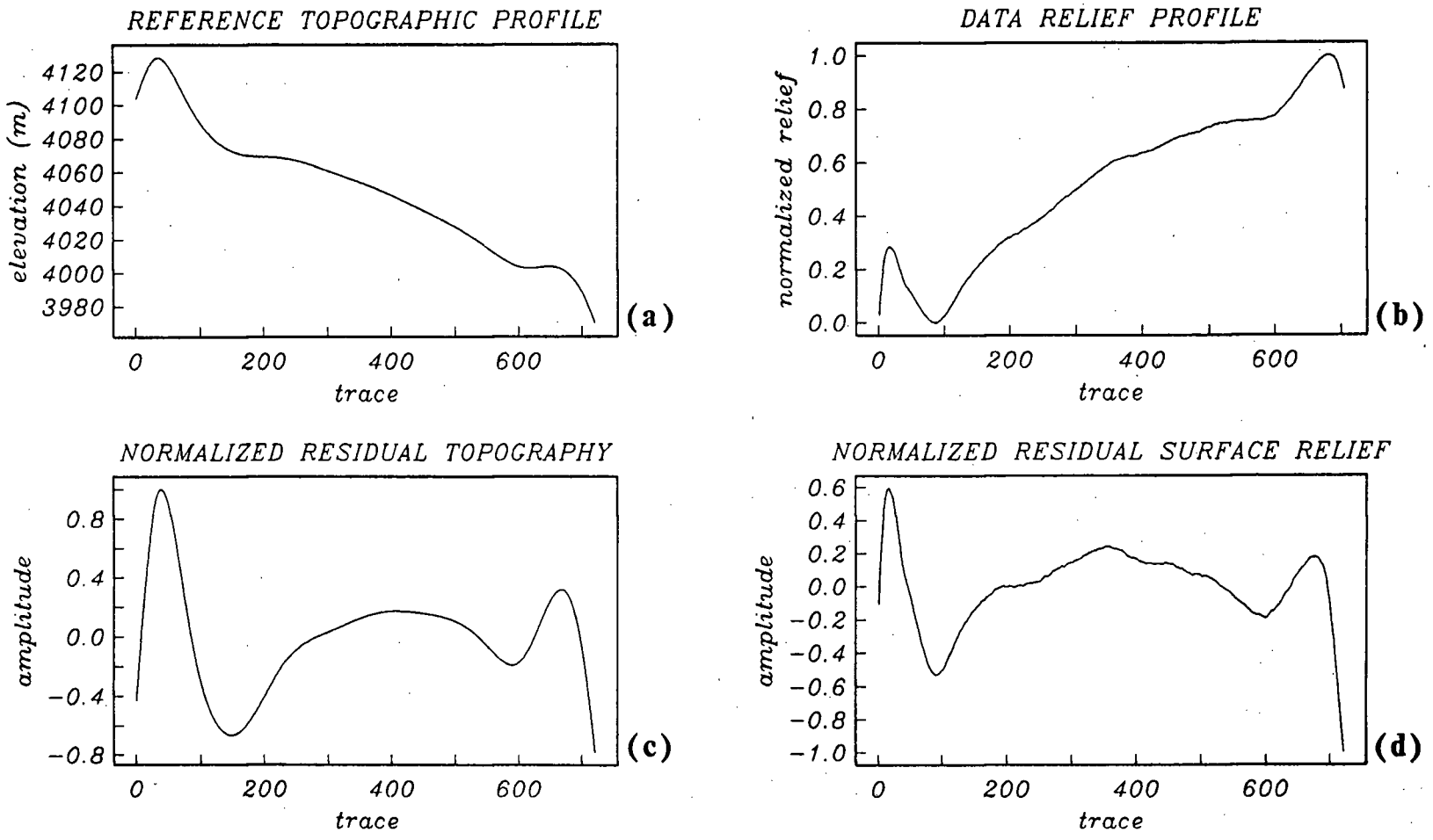

Figure 2.7. Compensation for gross linear flight trajectory. A strong linear flight gradient over the actual topography, (a), produces an apparent reversal of the relief trend recorded, (b). The trend reversal is compensated by removing the regional gradient from reference and data profiles. Corresponding residual profiles are obtained, (c) and (d).

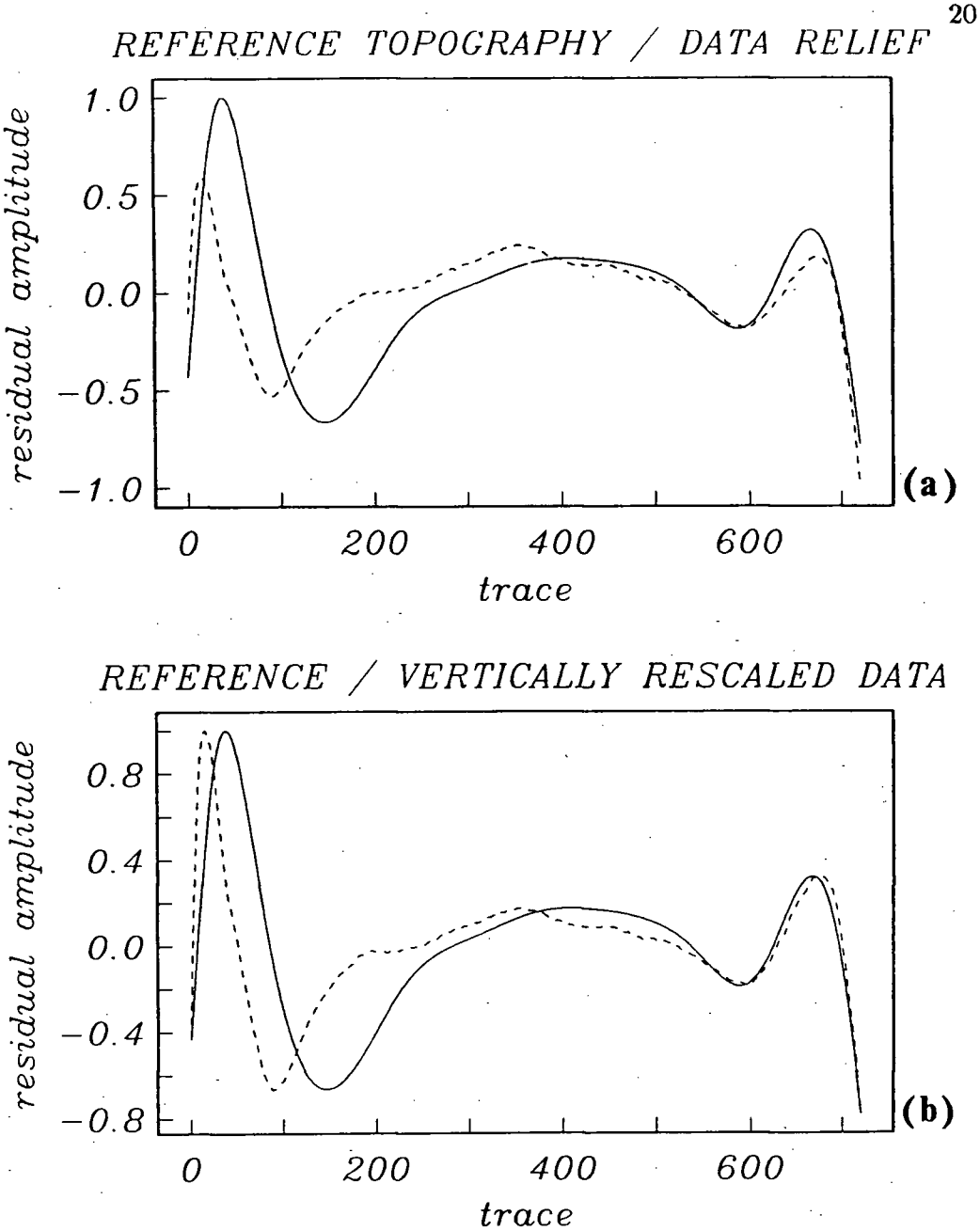

Figure 2.8. Vertical rescaling. (a) Comparison of normalized residual profiles. (b) The residual data profile is linearly rescaled relative to the reference profile between control features. Dashed and solid profiles represent data and reference profiles respectively.

sliding windows with midpoints r and d representing consecutive reference and data profile samples respectively (Figure 2.9). The coherency map is, thus, defined in terms of local semblance as

$$S(r,d) = \frac{\sum_{i=0}^{2m}\left(R_{(r-m+i)} + D_{(d-m+i)}\right)^2}{\sum_{i=0}^{2m}\left(R^2_{(r-m+i)} + D^2_{(d-m+i)}\right)}, \tag{2.2}$$

for $r, d = m+1, m+2, ..., N-m$, where N is the profile length, $m = ((l/2) - 1/2)$ is the window width and $R_{(r-m+i)}$ and $D_{(d-m+i)}$ represent reference and data profile amplitudes at samples $(r-m+i)$ and $(d-m+i)$ respectively. Semblance may be viewed as the ratio of combined energy to the sum of individual energies within the windows of comparison. An acute sensitivity to local amplitude diversity makes semblance a well suited criterion of profile likeness.

A second stage in the alignment process involves an augmented path-finding procedure for determination of the lateral warping function $[W_r(i), W_d(i)]$, with $i = 1, 2, ..., n$. The procedure optimizes a piece-wise linear path over the coherency map by locally maximizing the semblance level subject to dynamic programming constraints (Figure 2.10). In addition to imposing physically grounded restrictions upon allowable feature association, programming constraints significantly reduce necessary computations. Constraints are applied at both local and global levels and include:

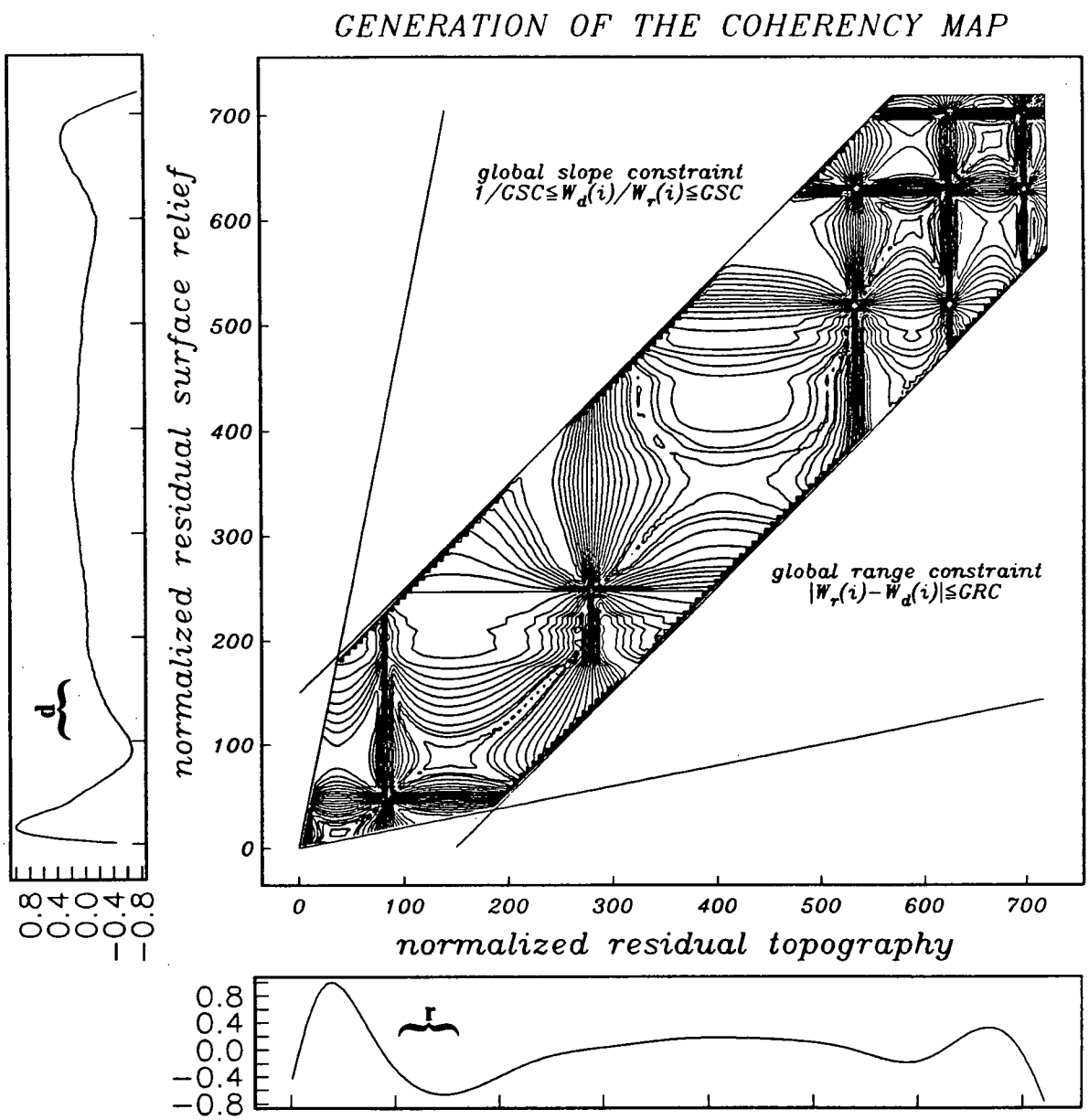

Figure 2.9. Generation of the coherency map. Residual reference and data profiles are compared over sample windows having midpoints r and d respectively. The coherency measure is calculated and entered at midpoint coordinates. The resulting coherency distribution is characterized by a well defined non-linear ridge that roughly determines the optimum warping function. Global path constraints restrict necessary computations.

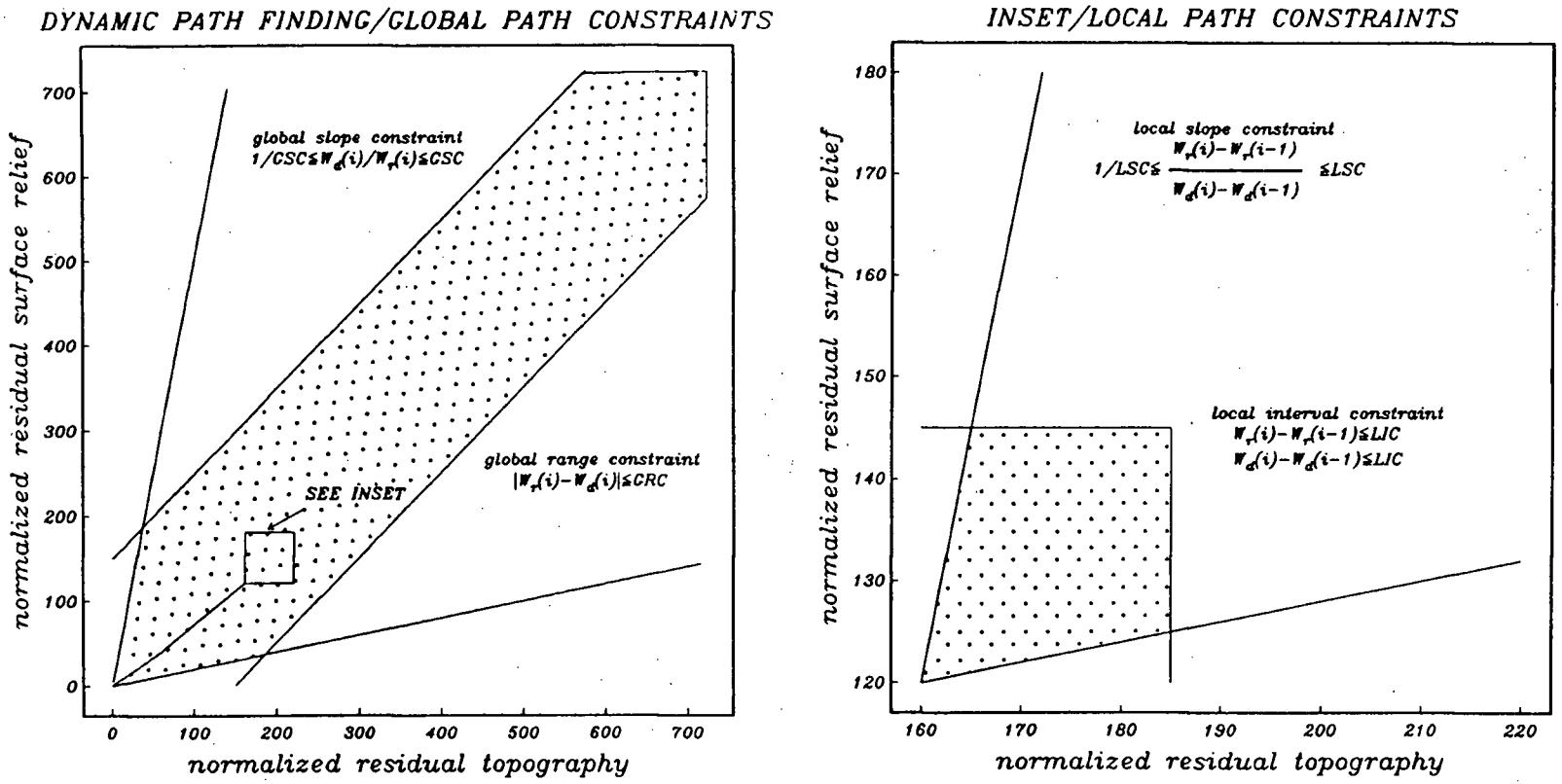

Figure 2.10. Dynamic programming constraints. Constraint boundaries are indicated by solid lines. Shaded areas define allowed search regions on both global and local levels.

Endpoint Constraint: The data relief profile and reference topographic profile are assumed to span an identical traverse segment. Despite spatial distortion of the data profile within the interval, endpoints are required to coincide. The endpoint constraint initiates and concludes the path-finding procedure by stipulating that

$$[W_r(i), W_d(i)] = [i, i], \qquad i = 1, 2, ..., m+1, n. \tag{2.4}$$

Local Slope Constraint: Fundamentally, the local slope constraint (LSC) requires that the path be extended in a monotonically non-decreasing fashion. More stringent restrictions are subjective and related to limitations upon aircraft acceleration and maximum expected distortion. The LSC is defined as

$$\frac{1}{\text{LSC}} \leq \frac{W_r(i) - W_r(i-1)}{W_d(i) - W_d(i-1)} \leq \text{LSC}, \qquad \text{i} = \text{m}+2, \text{m}+3, ..., \text{n}-1, \tag{2.5}$$

where LSC$\geq$1. An additional penalty-based constraint may be imposed in conjunction with the LSC. In effect, such a constraint involves the application of a local weighting template in favor of linear path extension. The local semblance level is scaled according to a weighting function of the form

$$S'(r,d) = \begin{cases} \delta^w S(r,d), & \delta \leq 0 \\ \delta^{-w} S(r,d), & \delta > 0 \end{cases}, \tag{2.6}$$

where $\delta = \big(d - W_d(i-1)\big)/\big(r - W_r(i-1)\big)$ is the local slope, w is a positive exponent governing penalty severity and $S'(r,d)$ is the scaled semblance.

Local Interval Constraint: The local interval constraint (LIC) imposes a maximum limitation upon step-size by requiring that

$$\text{LIC} \geq \begin{cases} W_r(i) - W_r(i-1), & i = m+2, m+3, ..., n-1 \\ W_d(i) - W_d(i-1), & i = m+2, m+3, ..., n-1 \end{cases}, \tag{2.7}$$

where LIC$\geq$1. In other words, the LIC restricts the range over which the procedure is allowed to "look ahead". Selection of the LIC involves a trade-off between accuracy and execution time.

Global Slope Constraint: The global slope constraint (GSC) is simply an extension of the LSC applied upon initiation of the procedure;

$$\frac{1}{\text{GSC}} \leq \frac{W_d(i)}{W_r(i)} \leq \text{GSC}, \qquad \text{i} = \text{m}+2, \text{m}+3, ..., \text{n}-1, \tag{2.8}$$

where GSC=LSC$\geq$1. Although the GSC does not directly influence the path-finding procedure, the constraint significantly reduces required computations.

Global Range Constraint: The global range constraint (GRC) restricts the maximum cumulative interval between data and reference profile samples required to coincide by the resulting warping function. The GRC reflects an estimate of maximum overall distortion by requiring that

$$\left| W_r(i) - W_d(i) \right| \leq \text{GRC}, \qquad \text{i} = \text{m}+2, \text{m}+3, ..., \text{n}-1, \tag{2.9}$$

where GRC$\geq$0.

Dynamic path-finding yields the non-linear warping function depicted in Figure 2.11. Application of the function affects relative compressions and extensions required to compensate spatial sampling errors and align the residual profiles (Figure 2.12). A final transformation involves the reversal of linear regression and normalization operations to obtain the corrected surface reflection profile.

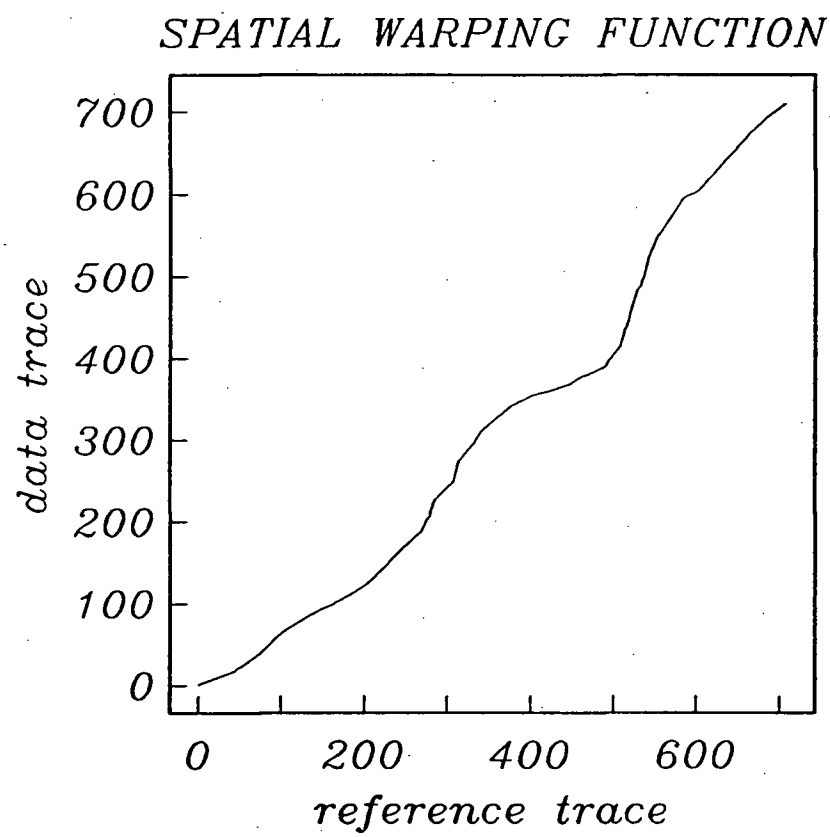

Figure 2.11. Spatial warping function determined by dynamic path-finding, subject to global and local constraints.

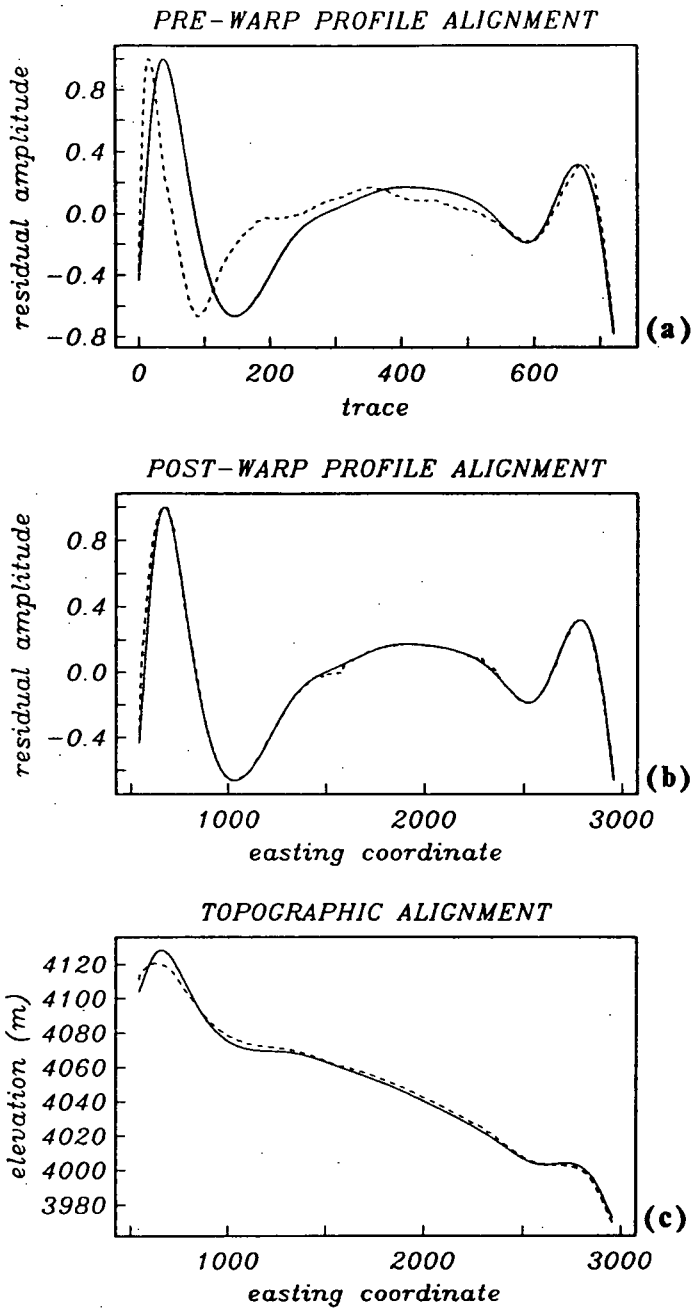

Figure 2.12. Application of spatial warping function. (a) Profile alignment prior to warping. (b) Profile alignment resulting upon application of the spatial warping function. (c) Profile alignment in topographic coordinates. Dashed and solid profiles represent data and reference profiles respectively.

2.3.4 Interpretation of the Warping Function

Realizing that the surface reflection profile and reference topographic profile are temporally and spatially sampled sequences respectively, the warping function is correctly interpreted as a time-distance relation. The derivative of the function is, thus, a continuous record of apparent ground speed along the traverse. Qualitatively, the interpretation roughly reflects the manner in which traverses were piloted. Quantitatively, the apparent ground speed is marginally unreasonable over certain intervals. Artificial inflations of the actual ground speed are the consequence of compensating residual altitude variations that are incorrectly handled as ground speed fluctuations. Despite gradient removal and amplitude rescaling procedures, small scale vertical distortions persist and pose a minor source of error in the waveform alignment procedure.

2.3.5 Conclusion

In addition to rectifying spatial distortions, the alignment process automatically positions individual data traces in northing, easting and elevation coordinates. The end result is a spatially accurate time section (Figure 2.13). Comparison of original and corrected versions emphasizes the necessity for spatial correction prior to interpretation. Although the procedure is presently adequate, a continuous record of aircraft altitude should replace linear regression and amplitude rescaling operations. Precision altimeters are available for moderate cost.

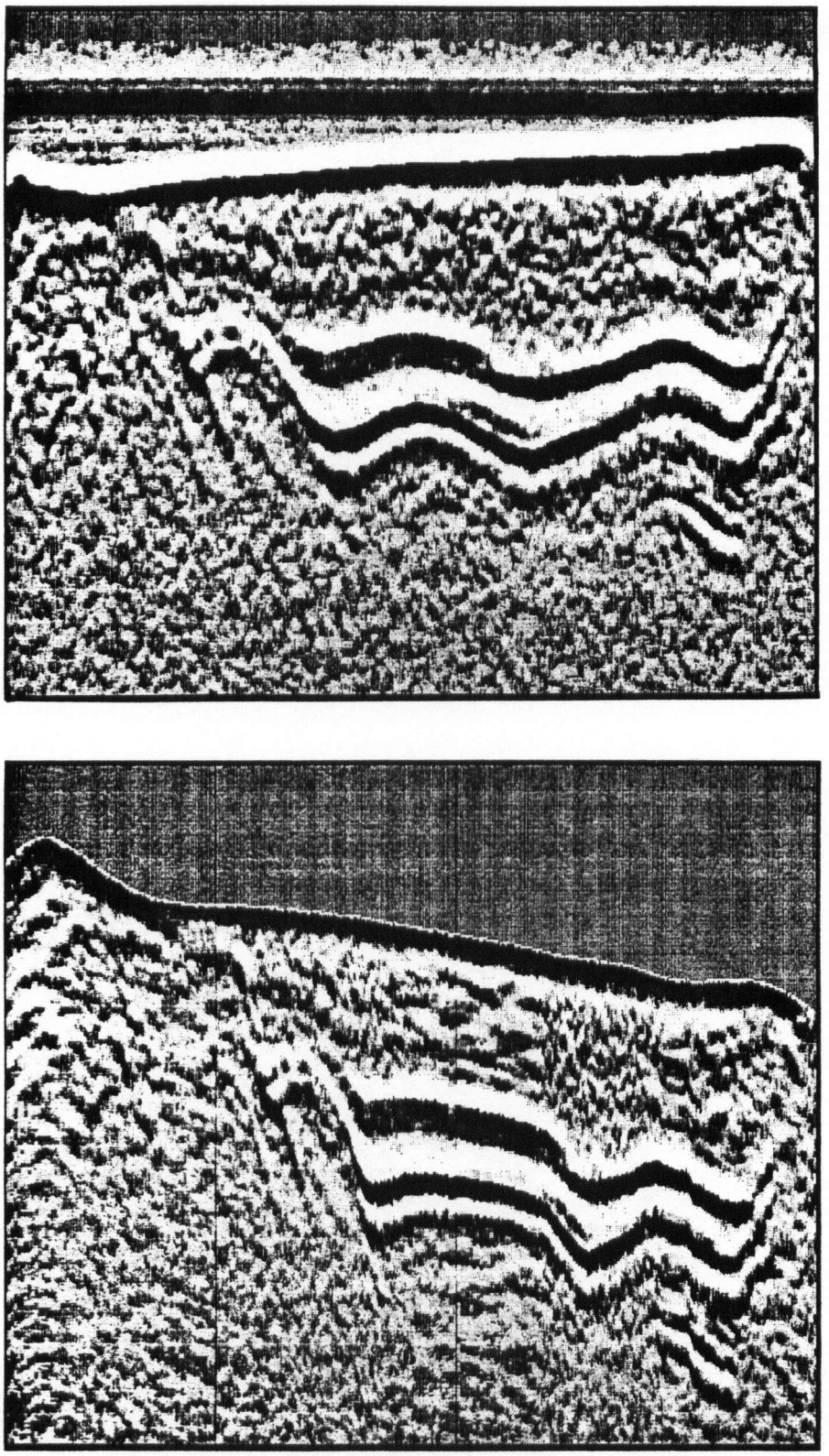

Figure 2.13. Effect of spatial corrections. (a) Enhanced time section. (b) Equivalent section following application of the warping function for compensation of spatial sampling errors.

2.4 An Interpretation Model and Time-Depth Conversion

2.4.1 Time-Depth Conversion

Although the surface reflection profile is spatially corrected by way of the dynamic waveform alignment procedure, the trailing data traces remain a function of time rather than depth. A final processing step involves time-depth conversion in the vertical coordinate to produce true cross-sectional records for interpretation. Conversion requires knowledge of the vertical variation in electromagnetic wave velocity with depth.

Electromagnetic wave velocity is given by

$$v_{em} = \frac{v_o}{\epsilon^{\frac{1}{2}}}, \tag{2.10}$$

where v_o represents the propagation velocity in free space and the relative dielectric permittivity, ϵ, is modelled as a function of density, ρ, according to an empirical relation due to Robin and others (1969);

$$\epsilon = (1 + 8.5 \times 10^{-4}\rho)^2. \tag{2.11}$$

Depth dependent density variation is turn described by a densification model proposed by Benson (1962) for snow/firn compaction on the Greenland Ice Sheet. According to Benson's model,

$$\frac{d\rho}{dz} = \begin{cases} m_1\rho^2\left(\frac{\rho_I-\rho}{\rho_I}\right), & p \leq p^* \\ m_2\rho^2\left(\frac{\rho_I-\rho}{\rho_I}\right), & p > p^* \end{cases}, \tag{2.12}$$

where p is the depth dependent ice pressure, ρ_I is the density of ice and m_1, m_2 and p^*, the critical pressure, are empirical constants. The two-way transit time, τ_2, for propagation to a given depth, z, is determined by integrating

$$\frac{d\tau_2}{dz} = \frac{2\epsilon^{\frac{1}{2}}}{v_o}. \tag{2.13}$$

The preceding equations are coupled with additional differential equations, glaciological measurements and empirical relations in a unified interpretation scheme developed to model depth dependent variation of interrelated physical properties within the caldera glacier.

2.4.2 Interpretation Model

The numerical interpretation model (Clarke and Benson, 1982; Clarke and others, 1987) yields the surface-normal depth dependent variation in temperature T, heat flux q, ice pressure p, density ρ, surface-normal component of flow velocity w, downslope component of flow velocity u, depositional age t_a, two-way propagation time τ_2 and two-way dielectric propagation loss P_2. In addition to Equations 2.12 and 2.13, the system of coupled linear differential equations includes:

$$\frac{dT}{dz} = -\frac{q}{K} \tag{2.14}$$

$$\frac{dq}{dz} = -\rho c w \frac{dT}{dz} + 2B_o \exp\left(\frac{-Q}{RT}\right)(F\rho \tan\alpha)^{(n+1)} + \frac{pw}{3\rho}\frac{d\rho}{dz} \tag{2.15}$$

$$\frac{dp}{dz} = \rho g \cos\alpha \tag{2.16}$$

$$\frac{dw}{dz} = -\frac{w}{\rho}\frac{d\rho}{dz} - \Delta \tag{2.17}$$

$$\frac{du}{dz} = -2B_o \exp\left(\frac{-Q}{RT}\right)(Fp\tan\alpha)^n \tag{2.18}$$

$$\frac{dt_a}{dz} = \frac{1}{w} \tag{2.19}$$

$$\frac{d\tau_2}{dz} = \frac{2\sqrt{\epsilon}}{v_o} \tag{2.20}$$

$$\frac{dP_2}{dz} = 2D, \tag{2.21}$$

where K represents the thermal conductivity, c the specific heat capacity, Q the creep activation energy, R the universal gas constant, F a shape factor, α surface slope, n the flow law exponent, g gravitational acceleration, D the propagation loss rate and $\Delta = (\partial u/\partial x + \partial v/\partial y)$ the horizontal flow divergence. The coupled differential equations are integrated, together with Equation 2.11 and the following additional property relations, using the Runge-Kutta method:

$$c(T) = 2115.343 + 7.7929(T - T_o) \tag{2.22}$$

$$K(\rho, T) = 2\rho K_I(T)/(3\rho_I - \rho) \tag{2.23}$$

$$K_I(T) = 2.1725 - 3.403 \times 10^{-3}(T - T_o) + 9.085 \times 10^{-5}(T - T_o)^2 \tag{2.24}$$

$$D(T) = D_o \exp(-E/RT), \tag{2.25}$$

$$\Delta = \begin{cases} \Delta_o, & 0 \leq z \leq z_s \\ 0, & z > z_s \end{cases}, \tag{2.26}$$

with T_o representing the surface temperature, K_I the thermal conductivity of ice, D_o a propagation loss constant, E the activation energy for dielectric loss, Δ_o the horizontal flow divergence determined at the surface and z_s a stagnation depth, below which horizontal divergence is assumed negligible.

2.4.3 Conclusion

The effect of time-depth conversion is illustrated in Figure 2.14. Ready transformation from time to depth section is another distinct advantage of the digital recording format over photographic recording. Various elements of the interpretation model are explained in greater detail where relevant in subsequent chapters.

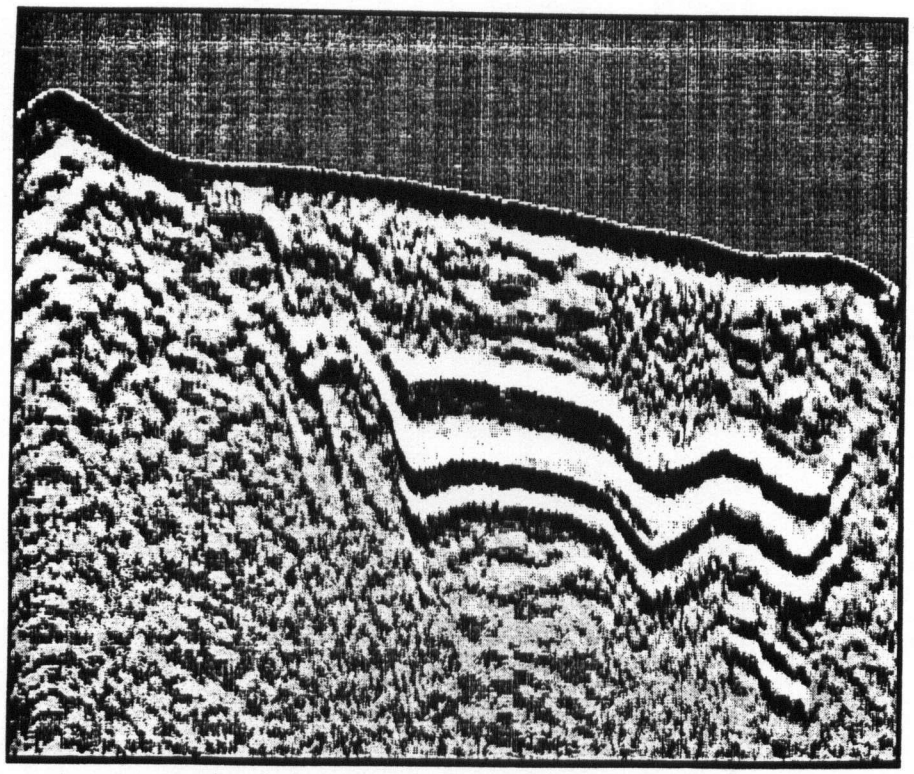

(a)

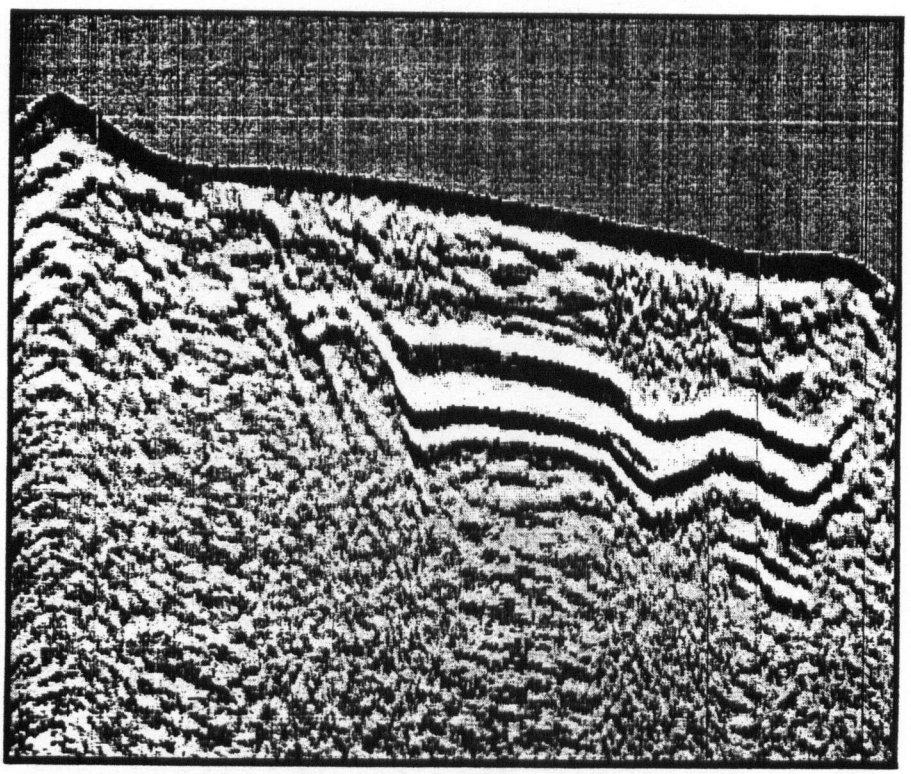

(b)

Figure 2.14. Effect of time-depth conversion. (a) Spatially corrected time section. (b) Spatially corrected depth section.

CHAPTER III

ICE THICKNESS AND SIGNAL ABSORPTION

3.1 Background

Ground-based radar probing experiments were conducted at Mt. Wrangell in 1976, 1977 and 1978 by the Geophysical Institute of the University of Alaska (Mackeith, unpublished; Motyka and others, 1980; Benson, 1982). Spot measurements of ice thickness were made in 1976 using a 5 MHz echo-sounder developed at the Geophysical Institute. Radio-echoes were consistently received from internal layers at approximately 90 and 200 m, and from the glacier bed to a depth approaching 450 m (Figure 3.1). Reflections from the bed were recorded near margins of the caldera only, suggesting that insufficient penetration prevented detection of echoes from greater depths. In 1977 the system antennas were modified to enhance sensitivity, and soundings were repeated in the central region of the caldera. A reflection recorded at a two-way time of 14.5 μs implies an ice thickness of 1250 m. Owing to poor directionality of the antennas, it was not ascertained whether the return was from the glacier bed, or surrounding terrain. The Scott Polar Research Institute's (SPRI) Mark IV equipment (Smith, 1971) was employed for similar ice thickness measurements in 1978. It was anticipated that improved directionality offered by the system would eliminate interfering reflections originating above the ice surface. Bed reflections were detected from depths approaching 900 m and consistent reflections from average depths of 225 and 350 m were attributed to internal layering. The maximum depth-sounding range achieved

with the Mark IV system suggested appreciably higher signal absorption rates than expected (Benson, 1982). An elevated volcanic impurity concentration was postulated to explain the anomalous absorption.

Re-analysis of reflections recorded in 1978 suggests an absorption loss rate of approximately 2.8 dB/100 m (Figure 3.2). In addition, the linear trend observed for reflections attributed to the glacier bed implies a power reflection coefficient (PRC) of -34 dB. In comparison, Robin and others (1969) suggested a minimum reflection coefficient of -22 dB for quartz-based materials. Although Smith (1971) concluded that bed roughness can effectively lower the PRC by as much as 10 dB, the above estimates of basal PRC and bulk loss rate may well be underestimated.

3.2 Analysis of Deep Reflections

The present investigation indicates the existence of three prominent reflecting horizons that are continuously detected over the caldera. Although reflections are intermittently received from above and below the major horizons, echoes are not recorded from depths exceeding 350 m. Results suggest that high signal absorption rates restrict detection of deeper horizons and, thus, that the lowermost continuous horizon should be interpreted as an internal layer rather than the glacier bed. The following lines of evidence support such an interpretation.

Over much of the recorded section, semi-continuous reflection events are detected below the horizon in question (Figure 3.3). Both isolated and stratified reflections are observed and found to extend laterally for distances approaching 750 m. Because geometrical considerations rule out multiple reflections as the source of deep-lying events, ice thickness must be at least equivalent to the maximum echo range. In

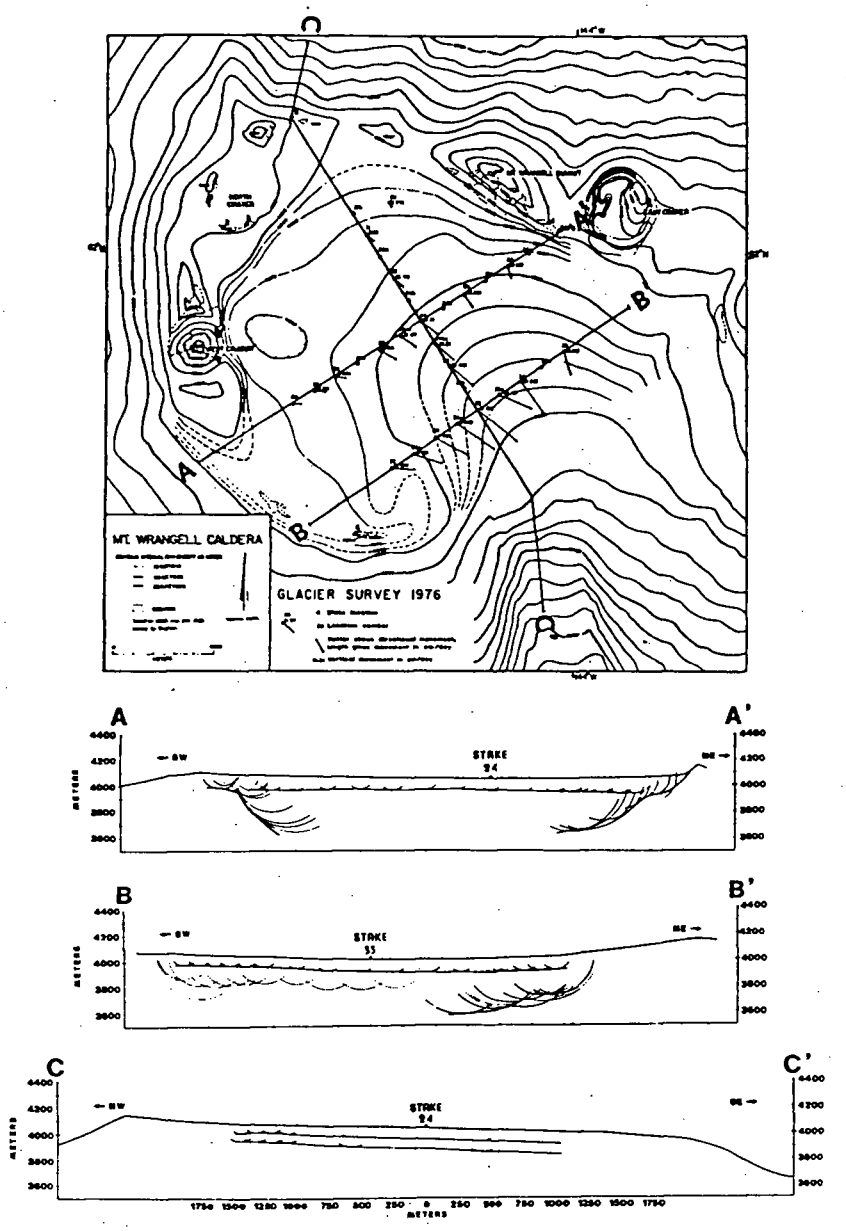

Figure 3.1. Preliminary interpretation of radio-echoes recorded in 1976. Vectors along survey lines indicate horizontal flow velocities measured during the same field season.

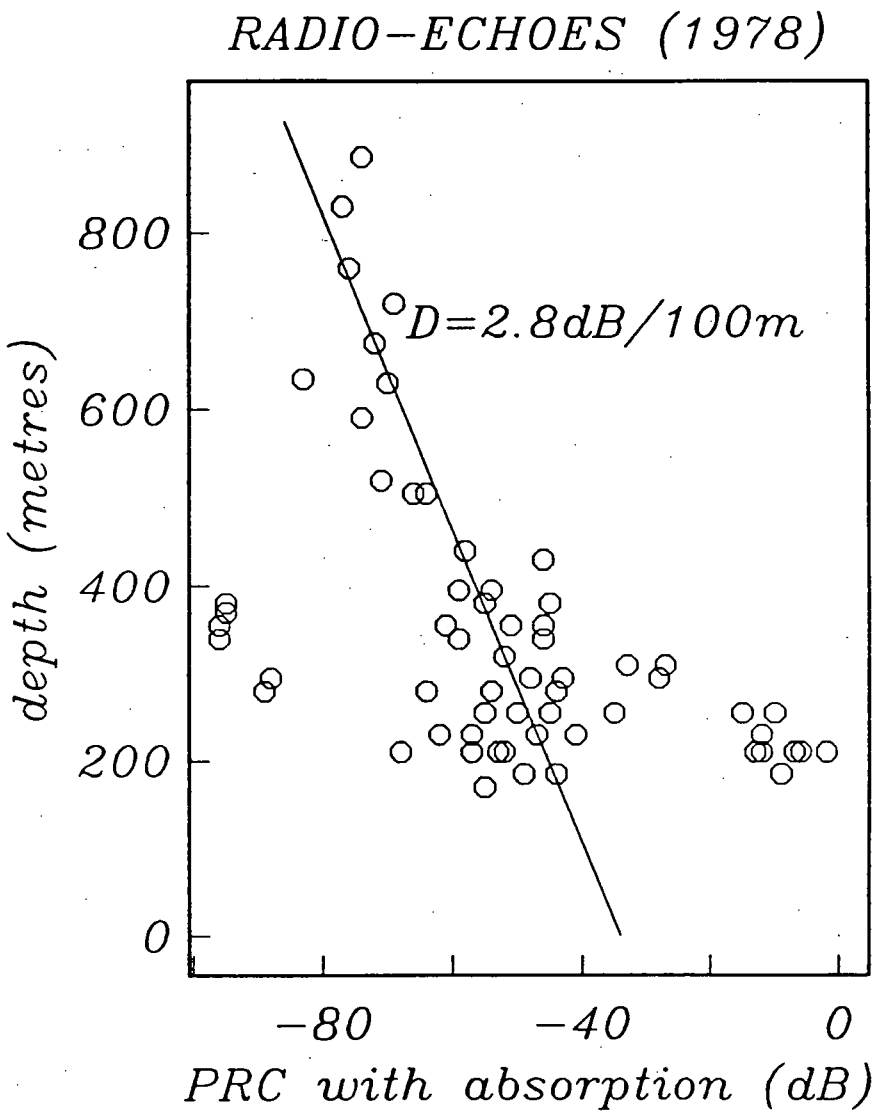

Figure 3.2. Radio-echoes recorded in 1978. The PRC, corrected for geometrical spreading, is displayed as a function of depth. Isolated clusters are attributed to internal layers. The remaining points exceeding 350 m depth are presumed to represent reflections from the glacier bed. Linear regression of these points suggests an absorption rate of 2.8 dB/100m.

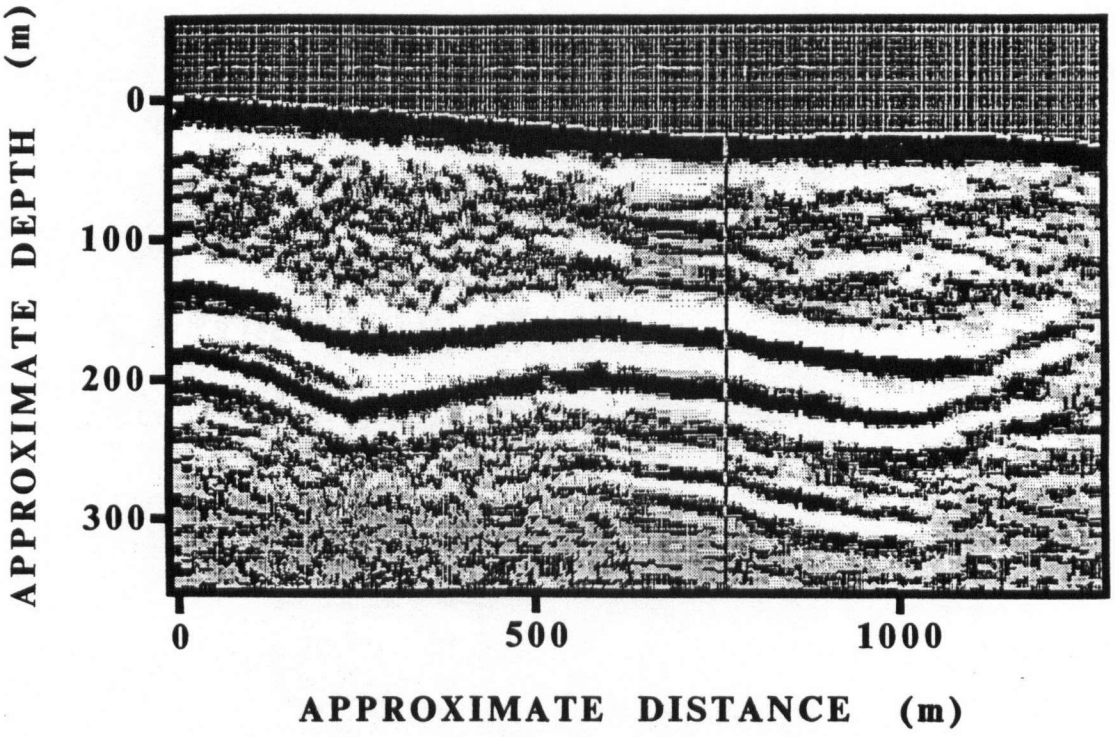

Figure 3.3. Portion of depth-section recorded over traverse-line A1, illustrating prominent reflection events below major horizons.

addition, statistical analysis of the power returned from major horizons demonstrates that the physical character of the lowermost horizon closely resembles that of overlying internal layers.

Roughness characteristics of reflecting interfaces have been interpreted on the basis of returned pulse shape and lateral variation in peak returned power (Harrison, 1972; Oswald, 1975; Neal, 1976; Millar, 1981a). Oswald (1975) examined the distribution of relative returned power for suites of closely spaced soundings of polar glacier beds. The distributions were interpreted as functions of sounding range and reflector roughness in terms of three dominant mechanisms for variation in returned power:

Interference: Where the sounding range is significantly greater than the radius of curvature for irregularities at the interface, numerous reflections are received simultaneously. Random interference of reflections results in rapid amplitude fluctuation at the receiver.

Focussing: Where the sounding range is roughly equivalent to the radius of curvature for irregularities at the interface, convergence and divergence of reflected radiation result in relatively smooth amplitude variation at the receiver (Harrison, 1971).

Pulse spreading: Where the sounding range is within the radius of curvature for deviations from a planar interface, relatively few reflections are received simultaneously. Amplitude variation at the receiver is related to the mean slope of irregularities.

To illustrate the present analysis, normalized relative power distributions are obtained for the three major horizons over a 200 trace range, representing a distance of approximately 600 m along traverse A10 (Figures 3.4, 3.5). The sample range is restricted by requiring that all horizons remain distinct over the interval. In addition, an interface between the outer flank of the caldera and the covering ice-pack is sampled for comparison. Examination of the resulting distributions (Figure 3.6) indicates that power returned from the three internal horizons tends to be distributed symmetrically about the mean; typically the result where pulse spreading effects dominate. Similar results are obtained for independent samples and suggest that the somewhat bimodal nature exhibited in the case of lowest horizon in Figure 3.6 is a feature of the particular sample only. In contrast, the power returned from the ice/bedrock interface is characterized by an asymmetric distribution, with deviations from the mean exceeding 20

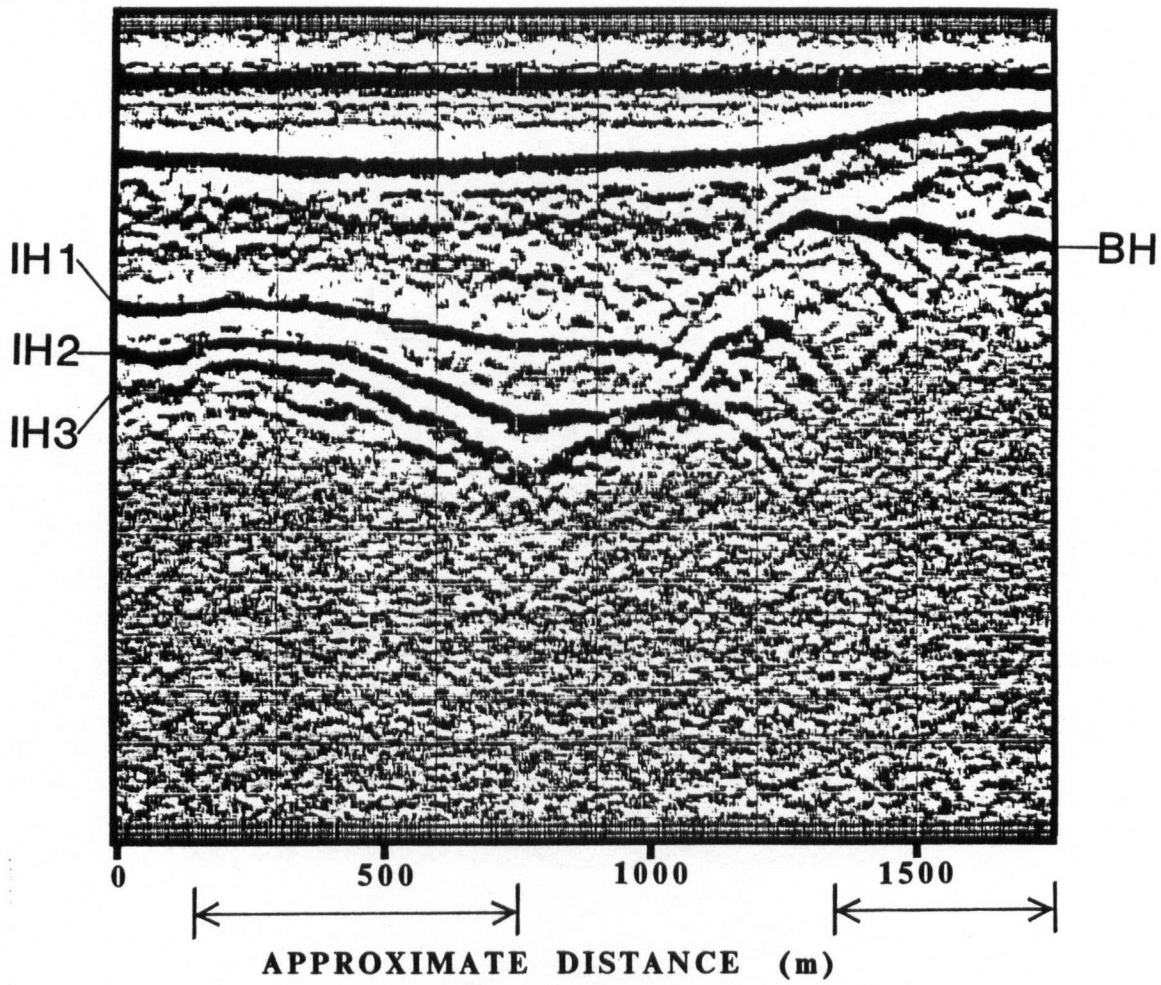

Figure 3.4. Portion of time-section recorded over flight-line A10. $IH1$, $IH2$ and $IH3$ denote major internal horizons. BH denotes the ice/bedrock interface. Arrows along the horizontal axis indicate ranges over which samples of the PRC were obtained for statistical analysis.

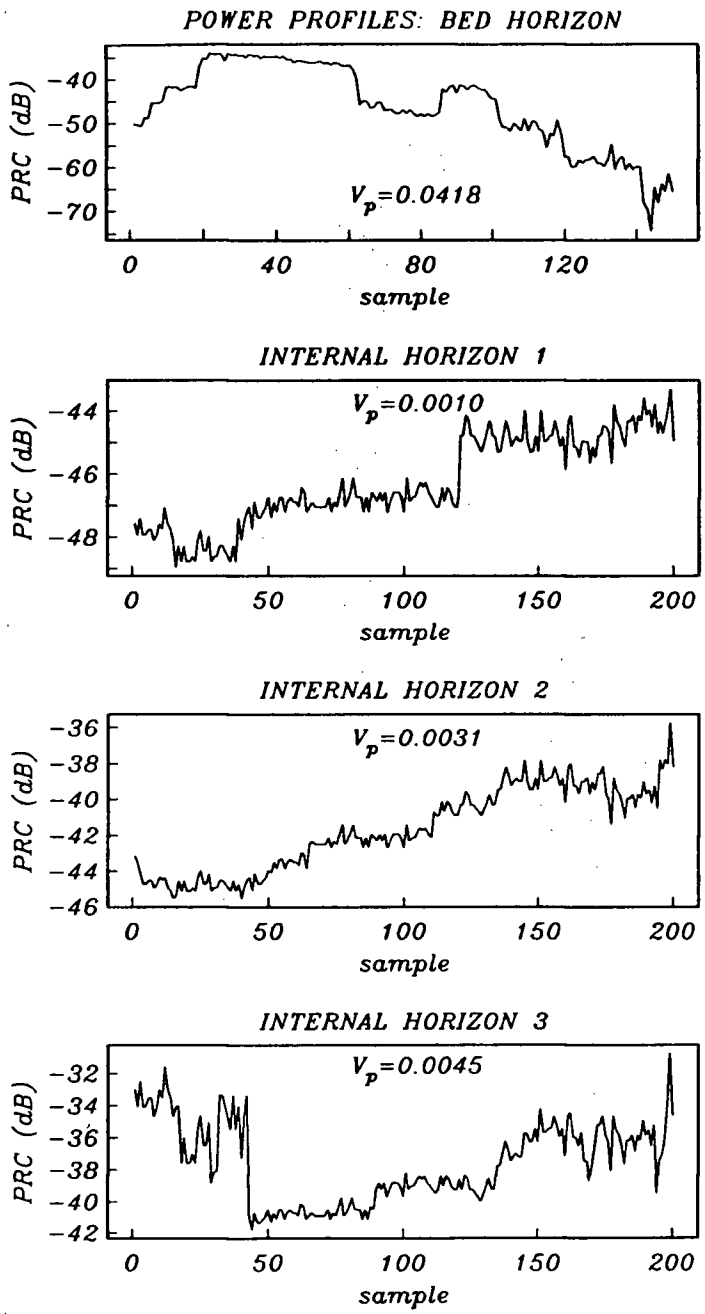

Figure 3.5. Power profiles obtained over sample ranges depicted in Figure 3.4. V_p is the normalized power variance.

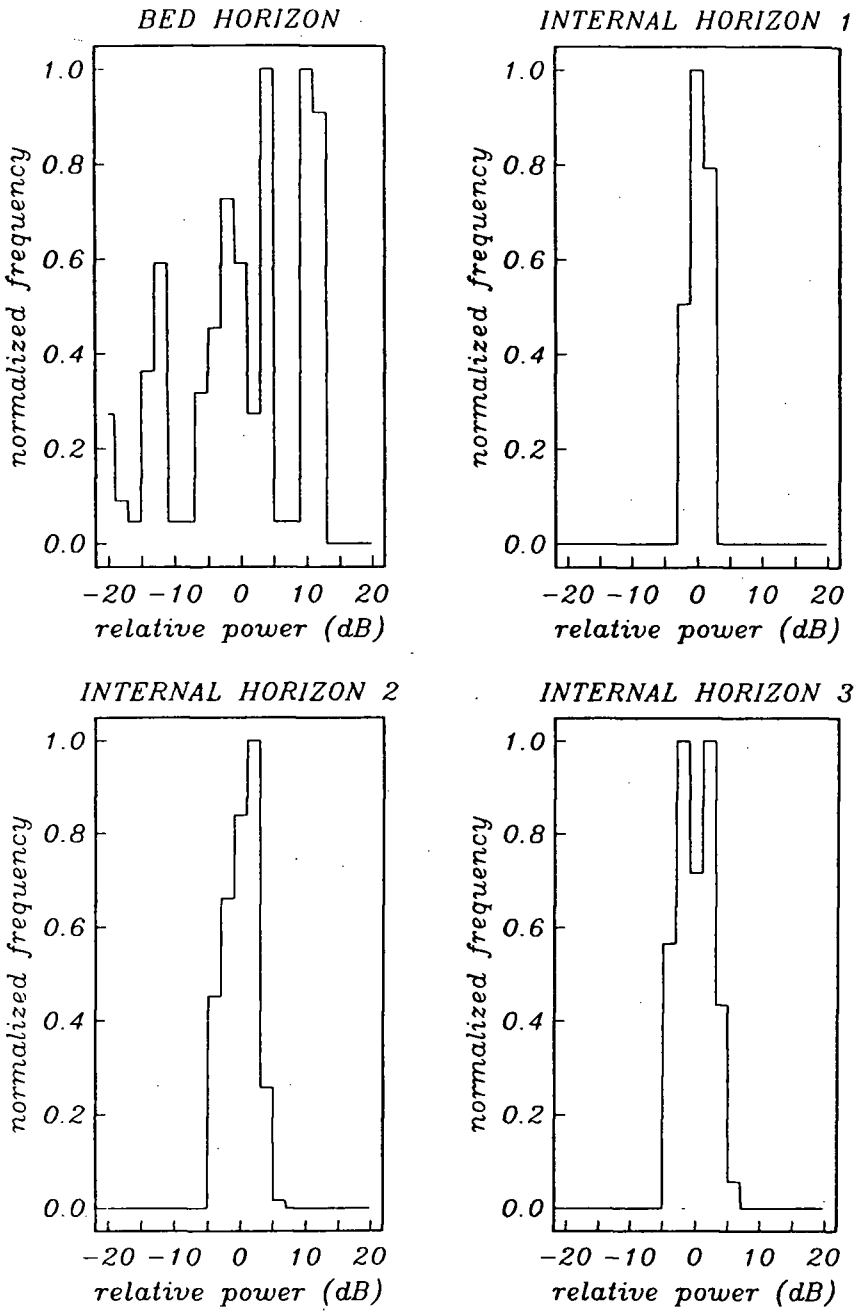

Figure 3.6. Normalized power distributions obtained over sample ranges depicted in Figure 3.4.

dB. Oswald (1975) demonstrated that such a distribution is expected in cases where interference is the dominant mechanism responsible for lateral variation in returned power.

Further evidence establishing the lowermost horizon as an internal layer is provided by comparison of the normalized power variance,

$$V_p = \frac{\langle P^2 \rangle - \langle P \rangle^2}{\langle P \rangle^2} = \frac{\langle P^2 \rangle}{\langle P \rangle^2} - 1, \tag{3.1}$$

where P represents returned power and angular brackets denote the spatial mean value. In every case studied, the normalized variance calculated for the lowermost horizon is found to agree roughly with the value for overlying internal layers (see Figure 3.5). Average normalized power variances for the three internal horizons are given in Table 3.1. In comparison, the average normalized variance for power returned from the ice/bedrock interface is approximately an order of magnitude larger. Average variance levels established for the three internal horizons are comparable to typical values tabulated by Neal (1977). Neal's values for an ice/bedrock interface exceed the average found here by another order of magnitude (Table 3.2).

3.3 Signal Absorption Rates

Assuming that the maximum ice-sounding range is limited by signal absorption, a rough estimate of the propagation loss rate is obtained using a modified form of the radar equation (Narod and Clarke, 1983),

$$P'_r = \frac{G^2 \lambda^2 R_A^2 T^2}{64\pi^2 r'^2} P_t \exp(-\mathrm{AC}) \exp(-2\mathrm{ADr_i}), \tag{3.2}$$

INTERFACE	$\overline{V}_p$
Internal Horizon 1	0.0012
Internal Horizon 2	0.0015
Internal Horizon 3	0.0028
Ice/Bedrock	0.035

Table 3.1. Average normalized power variances, $\overline{V}_p$, for prominent internal horizons and ice/bedrock interface at Mt. Wrangell. Values are determined over an average trace interval of 200 samples.

INTERFACE	SAMPLES	V_p
Internal Layer	360	0.007
Internal Layer	360	0.004
Ice/Bedrock	800	0.82
Ice/Bedrock	380	0.62

Table 3.2. Typical normalized power variances observed in polar studies (from Neal, 1977).

where G is the forward antenna gain; λ is the wavelength in air; R_A is the amplitude reflection coefficient for a plain reflecting target; T^2 is the power transmission coefficient at the air/ice interface (taken to be 1.0); P_t is the transmitted power and

$$r' = (r_a + \frac{r_i}{n}) \tag{3.3}$$

is the range adjusted for refraction, where n is the refractive index of ice and r_a and r_i are the range in air and ice respectively. The recorded power,

$$P_r' = P_r \exp(-\mathrm{AC}), \tag{3.4}$$

is the power received at the antenna, P_r, subsequently attenuated by internal losses, C, in decibels. D denotes the one-way propagation rate in decibels, and the conversion

factor, $A = (\log_e 10)/10$, is chosen such that $10 \log_{10} \exp(\mathrm{AD}) = \mathrm{D}$. At maximum range, the assumption $r_a << r_i$ is made and we obtain

$$10 \log_{10} r_{max}^2 + 2 \langle D \rangle r_{max} = 20 \log_{10} G + 10 \log_{10} \left(\frac{P_t}{P_r'} \right)_{max} + 20 \log_{10} \left[\frac{\lambda n T^2}{8\pi} \right] + 10 \log_{10} R_A^2 + \langle C \rangle , \qquad (3.5)$$

where bracketed variables denote decibel values. An estimate of the average one-way propagation loss rate in dB/100 m is, thus, given by

$$D = \frac{1}{200 r_{max}} \left[2 \langle G \rangle + \langle P \rangle + 20 \log_{10} \left[\frac{\lambda n T^2}{8\pi} \right] + \langle R_A^2 \rangle - 10 \log_{10} r_{max}^2 - \langle C \rangle \right], \qquad (3.6)$$

where $P = (P_t/P_r')_{max}$ is the system performance. Supplying the relevant system parameters and assuming an internal layer reflectivity of -45 dB, the effective propagation loss rate for a maximum range of 350 m is approximately 3.9 dB/100 m. A similar calculation yields a comparable loss rate of roughly 3.4 dB/100 m, corresponding to the maximum range of 900 m achieved with the SPRI 60 MHz equipment in 1978. A bed reflection coefficient of -30 dB is assumed for the latter estimate. Although use of a higher basal PRC improves the agreement between independent estimates, reanalysis of echoes recorded during the 1978 experiment suggests a reflection coefficient less than -30 dB. Recall that the loss rate estimated directly from the power-depth distribution is 2.8 dB/100 m (Figure 3.2).

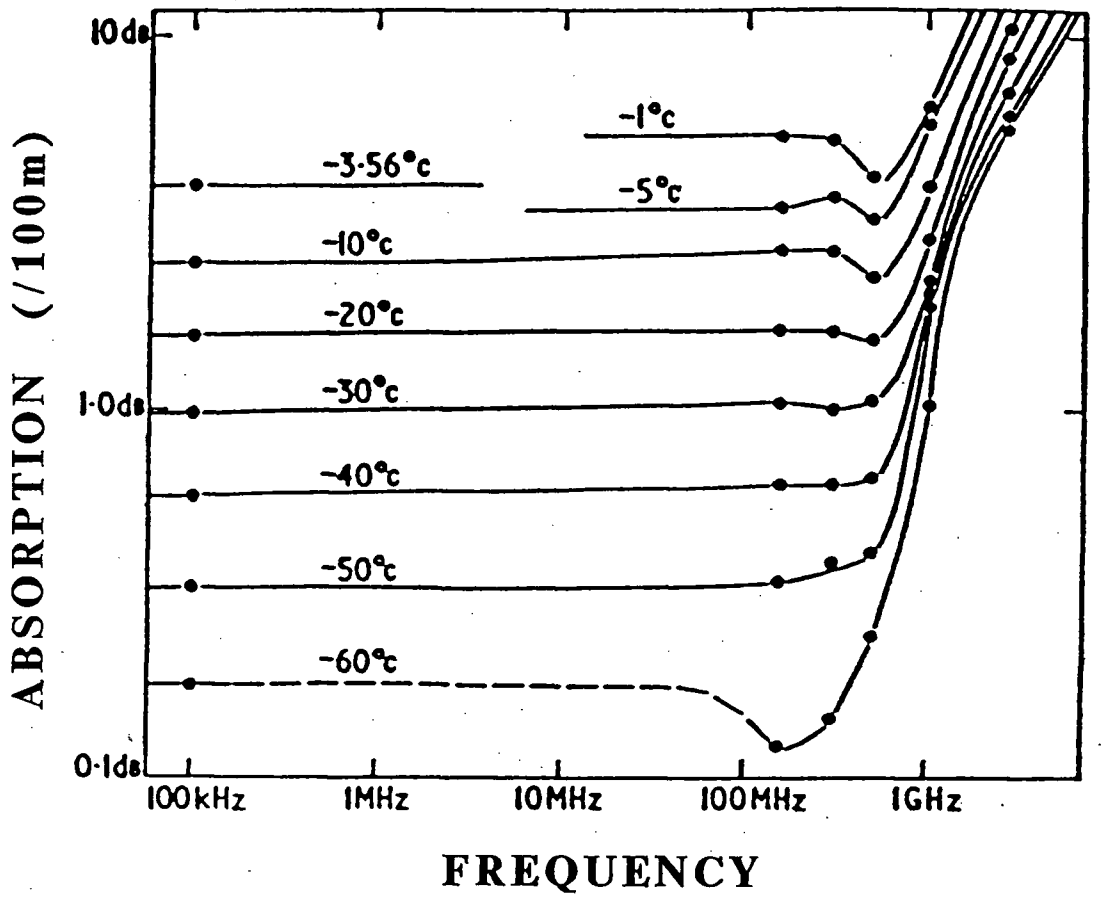

Figure 3.7. Absorption per 100 m in ice, as a function of frequency, with temperature as parameter (from Evans and Smith, 1969). Measurements at 100 KHz are due to Paren (1970) for samples from Camp Century, Greenland. Higher frequency measurements are due to Westphal (1963) for samples from Tuto Tunnel, Greenland.

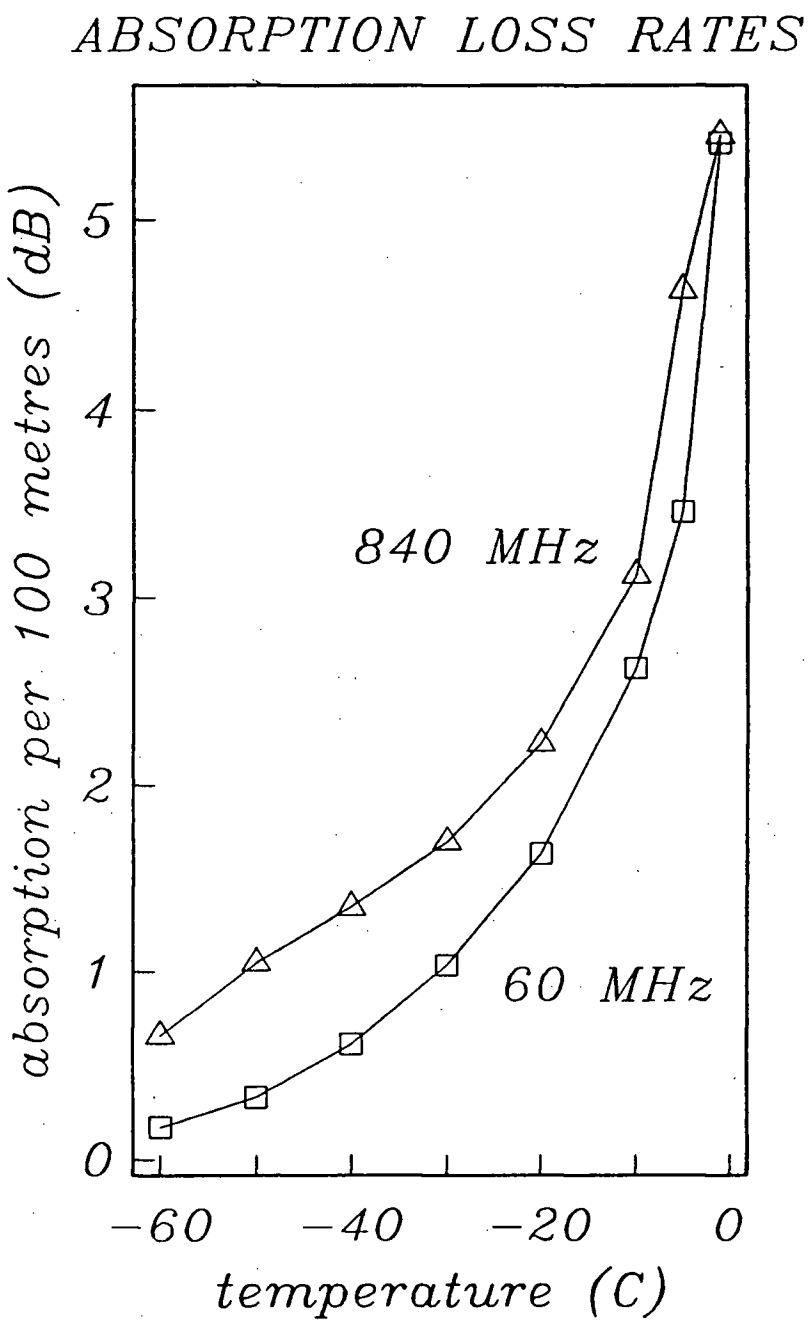

Figure 3.8. Absorption per 100 m in ice, at 60 and 840 MHz, as a function of temperature. Values were extracted from a digitized version of Figure 3.7.

Evans and Smith (1969) published a graphical compilation of laboratory measurements of dielectric absorption rates in polar ice (Figure 3.7). Absorption per 100 m path-length is displayed as a function of frequency over a range of ice temperature between -60 and -1 °C. For the present study, relevant absorption/temperature relationships are extracted at 60 and 840 MHz (Figure 3.8). Assuming Benson (1982) is correct in postulating an ice thickness of 900 m, an approximate vertical temperature distribution is calculated via the interpretation model. Corresponding predictions of the bulk loss rate at 60 and 840 MHz are obtained according to the respective absorption-temperature relationships for polar ice. In both cases, the predicted loss rate, 1.8 dB/100 m at 60 MHz and 2.3 dB/100 m at 840 MHz, is more than 1.5 dB below the estimate based upon maximum sounding range.

3.4 Estimation of Volcanic Impurity Concentration

According to Walford (1968), dielectric absorption in ice at frequencies between 0.1 and 100 MHz is due to dielectric relaxation. Deviations from the relaxation spectrum above a few hundred megahertz are attributed to the low frequency extreme of the infra-red absorption spectrum. Walford concluded that observed variations from the theoretical spectra are probably due to the effects of ionic impurities upon the dielectric relaxation mechanism. It is expected that high volcanic impurity levels are responsible for the difference between absorption rates at Mt. Wrangell and those observed for polar ice. Although no measurements of dielectric absorption exist for laboratory ice incorporating volcanic impurities, Millar (1981a; 1982) suggests that ice doped with hydroflouric acid (HF) is the nearest approximation. Camplin and others

(1978) analyzed the dielectric behavior of HF-doped ice and determined empirical relationships between HF impurity concentration and the high frequency conductivity, σ_∞, over a range of temperature. Millar (1981a) presented linear approximations of the form $\sigma_\infty = A\gamma + B$, where γ represents the HF concentration in moles per cubic metre (Figure 3.9). Appropriate coefficients for a given temperature and concentration range are supplied in Tables 3.3a,b.

TEMPERATURE (^oC)	A ($\times 10^{-3}$)	B ($\times 10^{-6}$)
-10	1.85	17.0
-20	1.75	6.0
-30	1.55	2.0
-40	1.15	1.0
-50	0.75	1.0

Table 3.3a. Linear coefficients for $\gamma < 0.01$ (see Figure 3.9).

TEMPERATURE (^oC)	A ($\times 10^{-3}$)	B ($\times 10^{-6}$)
-10	2.95	6.0
-20	1.95	4.0
-30	1.09	6.5
-40	0.58	7.0
-50	0.25	6.0

Table 3.3b. Linear coefficients for $0.01 < \gamma < 0.035$ (see Figure 3.9).

Upper limits on the bulk impurity concentration at Mt. Wrangell are obtained from maximum sounding range estimates of the propagation loss rate. The high frequency conductivity is given by

$$\sigma_\infty = 2\pi\epsilon_o\epsilon' f \tan\delta, \tag{3.7}$$

where ϵ_o is the permittivity of free space, ϵ' is the permittivity of ice and $f \tan \delta$ is the loss parameter. It is assumed that $\epsilon' = 3.17 \pm 0.07$ (Evans, 1965) and the loss parameter is

$$f \tan \delta = \frac{Dc}{2\pi\, 4.343 (\epsilon')^{\frac{1}{2}}}, \tag{3.8}$$

where D is the loss rate in decibels, c is the electromagnetic wave velocity in a vacuo and $4.343 = 10 \log_{10} e$. The interpretation model yields a mean temperature of approximately -10°C for an ice column 900 m thick. Using the appropriate coefficients, estimates of bulk volcanic impurity concentration are 0.010 and 0.012 mol/m^3 for soundings at 60 and 840 MHz respectively. These bulk levels are comparable to layer concentrations measured in polar ice cores, corresponding to major volcanic eruptions (Table 3.4).

ERUPTION	$[H^+]$ (mol/m^3)
Thera (1390 BC)	0.005
Eldja (934 AD)	0.020
Hekla (1104)	0.006
Laki (1783)	0.021
Tambora (1815)	0.008
Katmai (1912)	0.005

Table 3.4. Observed layer concentration of acids in polar ice sheets for known volcanic eruptions (From Millar, 1981b).

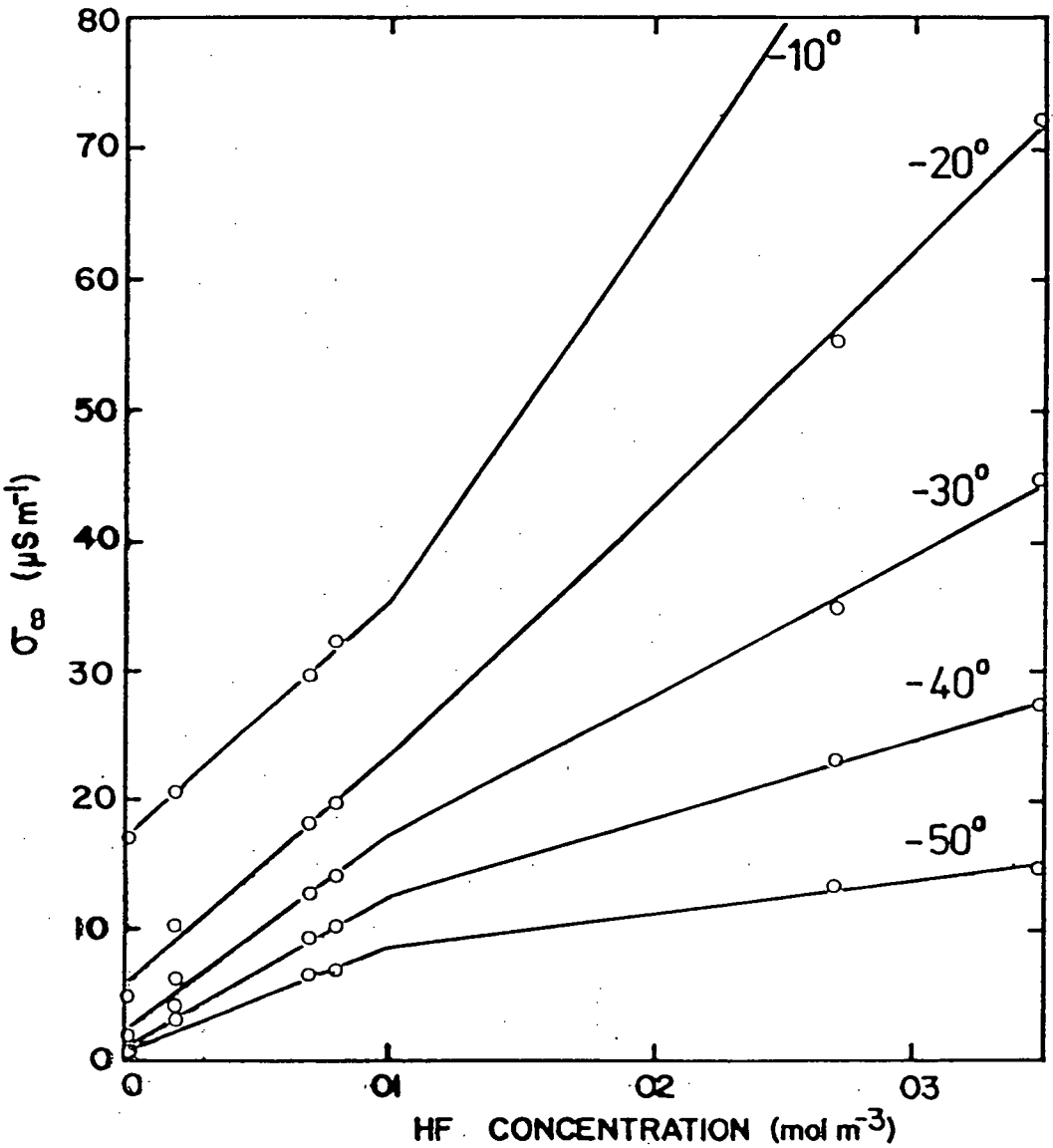

Figure 3.9. High frequency conductivity, as a bilinear function of HF concentration, with temperature as parameter (from Millar, 1981a).

3.5 Frequency-Selective Scattering Effects

A minor discrepancy between estimates of volcanic impurity concentration may reflect increased propagation losses due to scattering at the higher frequency. Although the particular mechanisms responsible are uncertain, a comparison of the relative magnitude of effects at 60 and 840 MHz is furnished by a hypothetical example. Smith and Evans (1972) modelled scattering from spherical ice inclusions within densified firn, according to a Rayleigh dependence upon frequency. Fractional power loss, per unit path length, due to scattering from m inclusions of radius b is

$$\delta = \frac{8\pi}{3} m b^6 \left(\frac{2\pi}{\lambda_o}\right)^4 \left[\frac{\epsilon_2(\epsilon_1 - \epsilon_2)}{\epsilon_1 + 2\epsilon_2}\right]^2, \tag{3.9}$$

where λ_o is the wavelength in a vacuo and ϵ_1 and ϵ_2 are the relative permittivities of ice and densified firn respectvely. The relative permittivity of densified firn is modelled according to an empirical relation given by Robin and others (1969),

$$\epsilon_2 = (1 + 8.5 \times 10^{-4}\rho_2)^2, \tag{3.10}$$

where ρ_2 is the firn density. Adapting a simple model for spherical ice lenses ($\rho_1 = 917.0$ kg/m^3, $\epsilon_1 = 3.17$) of radius 50 mm separated by 250 mm within a densified firn ($\rho_2 = 550.0$ kg/m^3, $\epsilon_2 = 2.15$), the predicted loss rate is approximately $0.5/\lambda_o^4$ dB/100 m. Considering radio propagation through numerous thin scattering layers of combined thickness 25 m, scattering losses at 840 MHz amount to 7.5 dB. Taken over a total ice thickness of 900 m, the total loss is represented by a bulk loss rate of 0.008 dB/100 m. In comparison, the scattering loss rate at 5 MHz is negligible.

3.6 Conclusion

High signal absorption rates, due primarily to volcanic impurities, restrict the present interpretation of ice thickness over the central region of the caldera. Statistical analysis of the peak power returned from reflectors at maximum range imposes a lower limit of 350 m upon maximum ice thickness. Although depth-soundings to 900 m with the SPRI Mark IV equipment are not confirmed, comparable estimates of the bulk loss rate at 60 and 840 MHz support the earlier findings. Reflections from the glacier bed are also uncertain in marginal regions of the caldera. Preliminary analysis, based upon statistics of peak returned power, suggests that dipping reflection events are mainly attributable to internal layers. In addition, the presence of distinct diffraction hyperbolae may indicate that the glacier bed descends sharply at the margins, causing reflections from the interface to be critically refracted. As a result, returns from the bed would not be detected above the ice surface. Estimates of maximum ice thickness reinforce such a conclusion by implying that the glacier bed must descend more steeply than observed reflections would indicate.

Despite suspected limitations on the interpretation of ice thickness, continuous depth-sectional coverage provides useful insight into caldera geometry and glacier volcano interaction. It is expected that, to a large extent, caldera structure may be inferred from the topography of internal horizons. Where this is not entirely the case, variations between the topography of internal horizons and the present ice surface might be related to heat flow distribution at the glacier bed. Finally, internal horizons are isochronal surfaces and suggest numerous interpretations of ice dynamics.

CHAPTER IV

RADIO-STRATIGRAPHY AND VOLCANIC HISTORY

4.1 Internal Reflection Mechanisms

The electrical character of dielectrics, including glacier ice, is described in terms of two fundamental properties: a complex relative magnetic permeability and a complex relative permittivity. Because ice is non-magnetic, the permeability is simply 1. The complex relative permittivity is given by

$$\epsilon^* = \epsilon' + i\epsilon'', \tag{4.1}$$

where the real part, ϵ', is simply referred to as the relative permittivity. Electromagnetic waves propagating through a dielectric are subject to partial internal reflection by inhomogeneities within the medium. The power reflection coefficient (PRC) associated with a dielectric discontinuity can be expressed in terms of a complex intrinsic admittance,

$$\Upsilon^* = \sqrt{\epsilon^*}. \tag{4.2}$$

For contrasting intrinsic admittances Υ_1^* and Υ_2^*, and assuming normal incidence upon a smooth interface, the PRC is given by

$$|R_A|^2 = \left| \frac{(\Upsilon_1^* - \Upsilon_2^*)}{(\Upsilon_1^* + \Upsilon_2^*)} \right|^2, \tag{4.3}$$

where R_A denotes the amplitude reflection coefficient (Paren, 1981).

Numerous physical mechanisms have been proposed to explain internal layer echoes. These mechanisms mainly involve relative permittivity contrasts caused by systematic fluctuations in the physical properties of ice, including density, crystalline anisotropy and bubble geometry (Robin and others, 1969; Harrison, 1973; Paren and Robin, 1975; Clough, 1977; Ackley and Keliher, 1979). Debris layers, containing dust and ash, have been discounted as a possible source mechanism on account of insufficient permittivity contrast. Although correlation between radio-echo soundings and ice core analyses support the previous mechanisms (Gudmandsen, 1975), there is no such evidence to suggest the importance of debris layers.

Density fluctuation is generally accepted as the most satisfactory explanation for internal reflections from above 1000 m. The predominant mechanism responsible for echoes originating from greater depths is less certain. Because the crystalline structure of ice is intrinsically anisotropic, Harrison (1973) suggested that an anisotropic relative permittivity might play an important role in the origin of deep reflections. Ackley and Keliher (1979) postulated that layered variation in bubble geometry, caused by deep-seated deformational processes, could enhance the PRC for coincident density contrasts. Paren and Robin (1975) investigated the importance of ionic impurity concentration and the distribution of impurity defects within the crystalline lattice. Unlike previously discussed mechanisms, ionic impurities affect the imaginary portion of the complex relative permittivity, ϵ'', which characterizes internal energy absorption due to the diffusion of lattice defects. Dielectric absorption is commonly described in terms of the loss tangent,

$$\tan \delta = \frac{\epsilon''}{\epsilon'}, \tag{4.4}$$

with the complex relative permittivity defined as

$$\epsilon^{*} = \epsilon'(1 - \tan\delta). \tag{4.5}$$

Because dielectric absorption is directly related to temperature, echoes resulting from variations in the loss tangent are expected to strengthen with depth.

Various atmospheric impurities enter the glacier system by means of condensation and precipitation. Stratified variations in impurity content within the ice mass, thus, reflect temporal fluctuations in the concentration of atmospheric contaminants. A combination of studies, involving trace element analysis (Boutron and Lorius, 1979) and conductivity measurements on melted ice cores from the Greenland Ice Sheet (Hammer, 1977; Hammer and others, 1980), have established acids of volcanic origin as the only common impurities that display variability in concentration on the scale required to produce observed reflections. Violent volcanic eruptions introduce large volumes of H_2S and SO_2 into the troposphere and stratosphere where subsequent chemical interaction with dominant atmospheric gases produces sulfate aerosols, particularly sulfuric acid (H_2SO_4). As a result of atmospheric mixing processes and ensuing "wash-out", global precipitation carries an elevated concentration of these volcanic impurities. According to Hammer (1977), precipitation deposited on the Greenland Ice Sheet has been found to possess an enhanced electrical conductivity for up to three years after the volcanic event of origin. Comparative studies of radio-echo soundings and ice core acidity profiles (Hammer, 1980; Millar, 1981a; 1981b; 1982) have confirmed a suspected cause-effect relationship between horizons of elevated volcanic impurity concentration and the radio-stratigraphy.

The depositional emplacement of volcanic impurities implies an isochronal interpretation of internal layering. A number of interesting glaciological problems have been approached from this perspective, including ice sheet stability (Whillans, 1976) and absolute dating of polar ice cores (Hammer and others, 1978). Although for present purposes internal layering at Mt. Wrangell is attributed purely to loss tangent variations, prominent horizons might well be due to a combined mechanism involving contrasts in both loss tangent and relative permittivity. For large-scale eruptive events, it is likely that major surface melting might accompany the deposition of volcanic acids, causing pronounced density layering in addition to increased impurity content.

4.2 Practical Estimation of Reflection Coefficients

Power reflection coefficients are calculated, as a function of range, according to a modified form of the "radar equation" presented in Section 3.3 (Equation 3.2),

$$P_r' = \frac{G^2\lambda^2 R_A^2 T^2}{64\pi r'^2} P_t \exp(-AC)\exp(-2ADr_i), \tag{4.6}$$

where G represents the forward antenna gain, λ the wavelength in air, R_A the amplitude reflection coefficient for a plain reflecting target, T^2 the power transmission coefficient (taken to be 1.0), P_t the transmitted power and $r' = (r_a + r_i/n)$ is the range adjusted for refraction, where n is the refractive index of ice and r_a and r_i denote the range in air and ice respectively. The recorded power, $P_r' = P_r \exp(-AC)$, is the power received at the antenna, P_r, susequently attenuated by internal system losses, C, in decibels. Recalling that $A = (\log_e 10)/10$ is a convenient conversion factor and D is

the propagation loss rate, in dB/m, the power reflection coefficient, $\langle R \rangle = 10 \log_{10} R_A^2$, is given by

$$\langle R \rangle = \langle P \rangle - 2 \langle G \rangle - 20 \log 10 \left[\frac{\lambda n T^2}{8 \pi r'} \right] + \langle Dr_i \rangle + \langle C \rangle , \tag{4.7}$$

where bracketed variables denote decibel values and $P = P_t / P_r'$ is the relative received power. Relative power is determined by calibrating the recorded signal over the dynamic range, relative to system performance. Propagation losses are modelled, via the interpretation model, according to a simple relationship governing a thermally activated loss mechanism,

$$D = D_o \exp \left(- \frac{E}{RT} \right) , \tag{4.8}$$

where T represents temperature, R is the universal gas constant and E, the activation energy, and D_o are empirical constants. The constants are determined by fitting the exponential relation to measurements of temperature dependent loss rate at 840 MHz (Westphal, 1963), subject to minimization of squared error (Figure 4.1). Two-way propagation loss, P_2, follows by integrating

$$\frac{dP_2}{dz} = 2D. \tag{4.9}$$

4.3 Composite Reflections and the Volcanic Record

While the radio-stratigraphy recorded at Mt. Wrangell is attributed to past volcanic activity, it is emphasized that the reflectivity record is expected to reflect gradual trends, as well as intermittent eruptive events. Due to atmospheric mixing processes, Antarctic and Greenland Ice Sheet stratigraphies record only major volcanic events

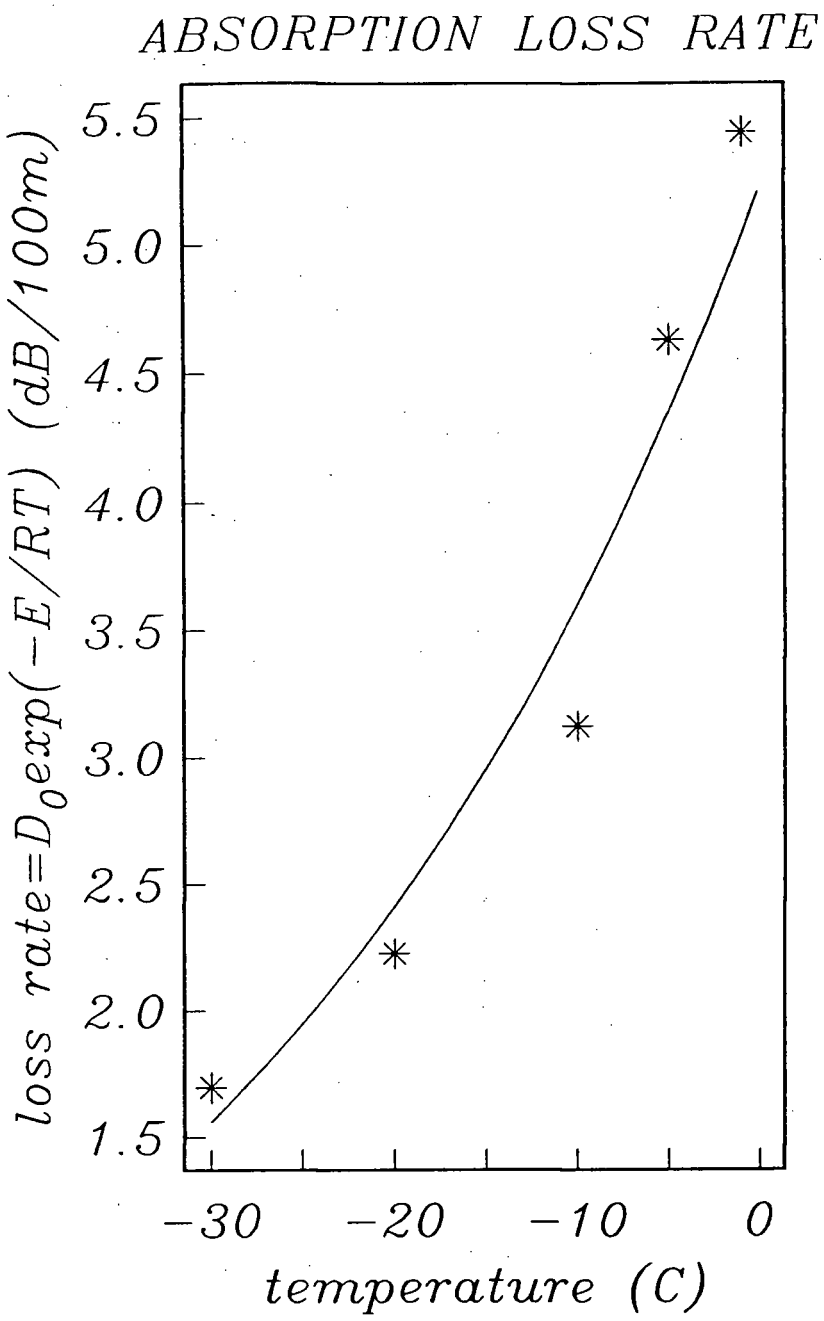

Figure 4.1. Absorption loss per 100 m at 840 MHz as a function of temperature. The loss rate is modelled according to a simple relationship for a thermally activated loss mechanism. The model distribution is depicted in relation to actual values extracted from a digitized version of Figure 3.7.

of global scale. The Mt. Wrangell stratigraphy, on the other hand, could quite conceivably reflect minute variations in activity, occurring over a matter of days. While stratification on such a scale is not resolved by radio-echo sounding, it is important to consider the possible effects of such layering. It has been suggested (Harrison, 1973; Clough,1977; Millar, 1981) that in situations wherein layer thickness and separation are comparable to the spatial pulse length, interference effects give rise to composite reflections with power levels exceeding those due to isolated interfaces. The reflection coefficient for a composite reflection is statistically dependent upon average layer properties over the pulse length.

Radio-reflections are caused by contrasts in the complex relative permittivity,

$$\Delta\epsilon^{*} = \Delta\epsilon' - i\epsilon'\Delta(\tan\delta), \tag{4.10}$$

where ϵ' is the relative permittivity and $\Delta\epsilon^{*}, \Delta\epsilon'$ and $\Delta(\tan\delta)$ denote variation in the complex relative permittivity, relative permittivity and loss tangent respectively. Harrison (1973) derived a general expression for the amplitude reflection coefficient due to fluctuation in relative permittivity, $\Delta(\tan\delta) = 0$, and considered three models for depth dependent variation, $\epsilon' = \epsilon'_1 + \Delta\epsilon'(z)$, where ϵ'_1 is the mean and $\Delta\epsilon' << \epsilon'_1$:

1. Isolated thin layers at spacings greater than the pulse length.

2. A random variation with depth, where $\Delta\epsilon'$ is statistically stationary over the depth of the medium (average properties remain constant).

3. A random variation with depth, where $\Delta\epsilon'$ is statistically stationary over distances of the same order as the pulse length (average properties smoothly variable on a scale large with respect to pulse length).

For an isolated thin layer of thickness l, Harrison obtained an expression previously given by Robin and others (1969);

$$R = |R_A|^2 = \frac{\pi^2 l^2}{\lambda_m^2}\left(\frac{\Delta\epsilon'}{\epsilon_1^2}\right)^2, \tag{4.11}$$

where R is the power reflection coefficient, R_A is the amplitude reflection coefficient and λ_m is the wavelength in the medium. The corresponding expression for stationary random variations is

$$R = \frac{\pi^3 p_m}{\sqrt{8}\lambda_m^2\left(\frac{1}{l^2}+\frac{2}{p_m^2}\right)^{\frac{1}{2}}}\left\langle\left(\frac{\Delta\epsilon'}{\epsilon'}\right)\right\rangle \exp-\left[\frac{k_m^2}{\left(\frac{i}{l^2}+\frac{2}{p_m^2}\right)}\right], \tag{4.12}$$

where p_m is the spatial pulse width in the medium, k_m is the wavenumber in the medium, angular brackets denote the ensemble average and the characteristic layer spacing, l, is modelled as the correlation length of $\Delta\epsilon'$, according to a Gaussian autocorrelation function of the form

$$\rho_\epsilon(\varsigma) = \exp\left(\frac{-\varsigma^2}{l^2}\right) = \frac{\int_{-\infty}^{+\infty}\Delta\epsilon'(z)\Delta\epsilon'(z+\varsigma)dz}{\int_{-\infty}^{+\infty}(\Delta\epsilon'(z))^2 dz}. \tag{4.13}$$

Harrison demonstrated that at any instance, power received at the antenna is the result of a trade-off between isolated and composite effects. According to Equation 4.12, the apparent spacing of reflections caused by composite effects tends to resemble either the pulse width, p_m, or the actual layer spacing, l, whichever is larger. In addition, it is found that for $l << p_m$ the composite reflection coefficient exceeds that for an equivalent isolated contrast by approximately the number of layers within a pulse width, p_m/l.

Of particular interest here is the final model, which constrains $\Delta\epsilon'$ to be statistically stationary on the scale of a pulse length, while allowing for smooth variation in average properties on a broader scale. Although Harrison focussed upon depth dependent thinning of layers caused by densification and deformation, this effect is given only secondary consideration in the present interpretation. Instead, gradual variations in stratified layer properties are mainly attributed to periodic trends in volcanic activity at Mt. Wrangell. It is assumed that depth-dependent variability in complex relative permittivity is due to gradual fluctuations in the pulse-width-averaged loss tangent. Mean trends in dielectric absorption are, in turn, attributed to average variations in volcanic impurity concentration. As a result, fluctuations in mean complex relative permittivity are given by

$$\Delta \langle \epsilon^*(z) \rangle = -i\epsilon' \Delta \langle (\tan\delta)(z) \rangle , \tag{4.14}$$

with

$$\Delta \langle (\tan\delta)(z) \rangle = \frac{\Delta \langle \sigma_\infty(z) \rangle}{2\pi\epsilon_o\epsilon' f}, \tag{4.15}$$

where ϵ_o is the permittivity of free space, f is the sounding frequency and $\Delta\langle\epsilon^*(z)\rangle$, $\Delta\langle(\tan\delta)(z)\rangle$ and $\Delta\langle\sigma_\infty(z)\rangle$ denote fluctuations in the depth dependent ensemble average of complex relative permittivity, loss tangent and high frequency conductivity. Relative permittivity, ϵ', is assumed constant and the high frequency conductivity is related to volcanic impurity concentration as discussed in Section 3.4. Although variations in ionic impurity content are assumed to be a direct result of temporal fluctuations in volcanic activity, it is necessary to realize that various post-depositional processes influence the glacio-volcanic stratigraphy. Consequently, to investigate the proposed dependence upon volcanic activity, it is useful to examine the variability in reflector strength as a function of depositional age, rather than depth. The relationship between depositional age and stratigraphic depth is determined by modelling the downward transport of surface-deposited precipitation (details are given in a subsequent section). Although this vertical coordinate transformation helps to illustrate our interpretation, the effects of post-depositional thinning upon the radio-stratigraphy are neither faithfully nor completely counteracted.

A spatially-averaged profile of the power reflection coefficient as a function of depositional age is depicted in Figure 4.2. Neglecting high frequency fluctuations, a gradual periodic trend in returned power is evident. It is suggested that this observation supports the proposed relationship between depth-dependent variation in complex relative permittivity and large scale trends in volcanic activity. Intermittent eruptive events, of relatively short duration, give rise to isolated layer effects superimposed upon the broad trend in returned power. Because post-depositional processes result in a gradual thinning of layers, isolated layer effects are most pronounced within the near surface region. On the other hand, since composite reflection strength exceeds that due to

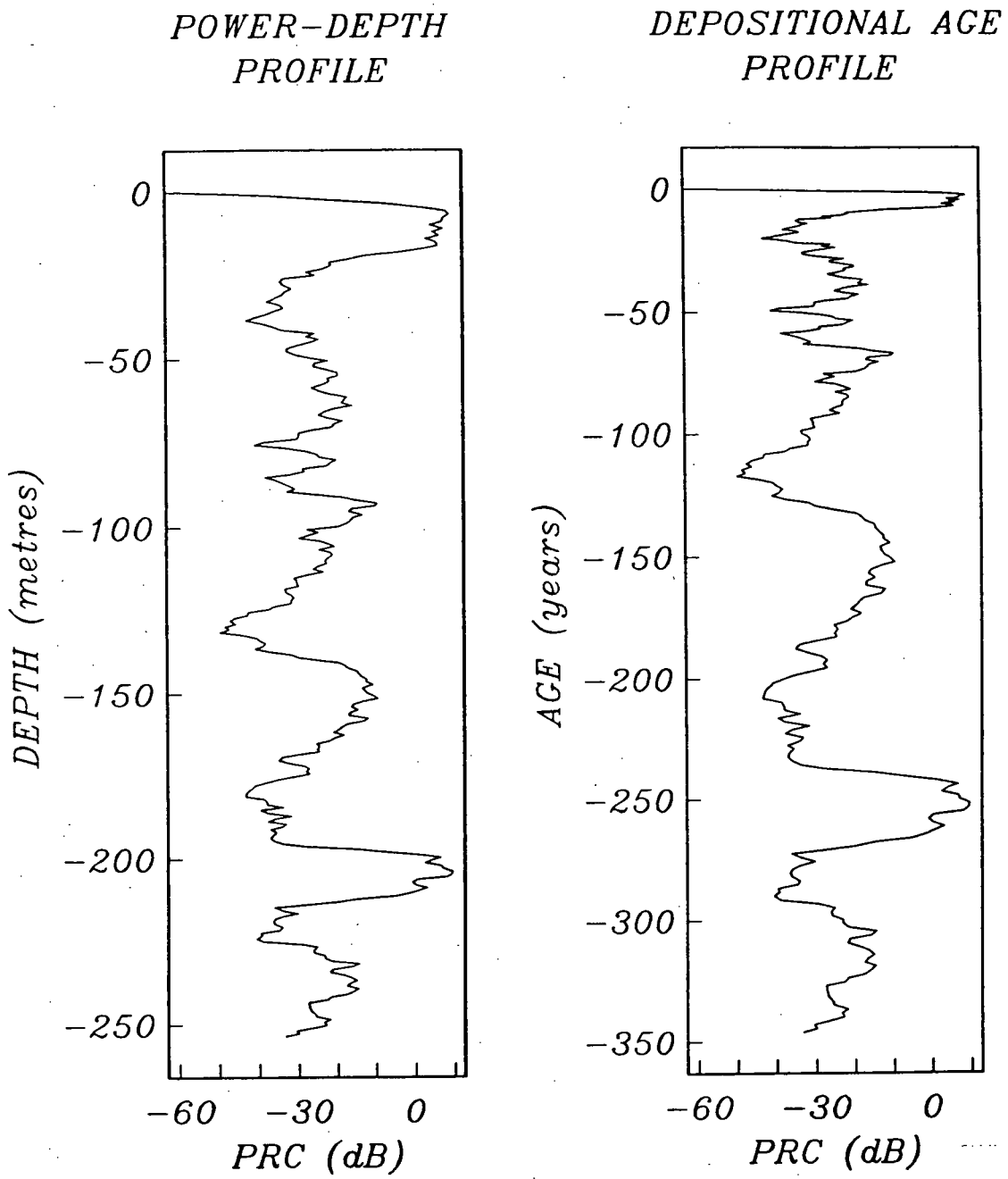

Figure 4.2. Spatially averaged power-depth profile with corresponding depositional age profile. Negative values imply depth below surface level and age relative to zero surface age. Positive power reflection coefficients are due to approximations inherent in corrections for geometrical spreading and absorption.

an equivalent isolated layer by roughly the number of layers within a pulse width, the average PRC is expected to increase with depth. A simultaneous increase in lateral layer continuity indicates the growing prominence of composite effects. Although local inhomogeneities can occur in the deposition of volcanic impurities, the average concentration is expected to be laterally homogeneous. Clough (1977) emphasized that, in addition to a dependence upon depth-averaged properties, the composite reflection coefficient is a function of pulse width-averaged properties over an individual horizon. As a result, in comparison to isolated layer reflections, composite reflections are expected to display relatively greater lateral continuity.

Millar (1981a) examined lateral continuity and structure of reflecting horizons recorded over the Greenland Ice Sheet. Apparent radio-echo separation was observed to increase with local thickening of the ice sheet. Where local layer separation exceeded the pulse length, an additional echo gradually emerged midway between the original horizons. Internal layering recorded near the southern rim of the caldera exhibits similar effects where the radio-stratigraphy undergoes pronounced down-warping (Figure 4.3). Two factors could explain the observed warping. First, by impeding downslope flow below a stagnation depth, roughly coinciding with ice thickness at the head of Long Glacier, the southern rim could cause the glacier fabric to buckle. Outflowing ice provides the necessary driving mechanism by concentrating shear stress below the stagnation depth. Secondly, anomalous volcanic heat flux at the caldera floor could cause a relatively rapid subsidence of glacier strata in the particular region. It is interesting to note that recent volcanic activity has concentrated along the opposite rim, to the north. Consequently, the question of anomalous heat flux below the southern rim hinges upon whether surface activity is related to a relative surplus

or depletion of the volcanic heat source. Regardless of the explanation for observed warping, the radio-stratigraphy is strongly influenced by the deformation. Figure 4.4 traces the progression of apparent reflections from a simple flat-lying configuration, detected within the central region of the caldera, to that observed near the southern rim. Close inspection of layer separation and continuity reveals a complex interplay between neighbouring horizons that appears to confirm the composite nature of deep reflections. Interference effects are analogous to those described by Millar and suggest an average thickening of glacial strata within the synclinal structure. Because apparent layer separation is inconsistent and does not appear to be directly controlled by pulse length, it is possible that the composite reflection mechanism involves the interference of multiple internal reflections. Although speculation along these lines requires further investigation, the foregoing analysis cautions against naive interpretation of deep-lying reflection horizons in terms of volcanic history.

4.4 Speculation on Volcanic History

4.4.1 Determination of Depositional Age

Although a permanent record of volcanic activity is preserved within the glacio-volcanic stratigraphy at Mt. Wrangell, several post-depositional processes influence the relationship between depositional age and stratigraphic level. Clearly, there exists a fundamental connection between the age of a particular layer and the rate at which that horizon proceeds vertically downward, relative to the active glacier surface. The vertical transport of surface deposited precipitation involves densification,

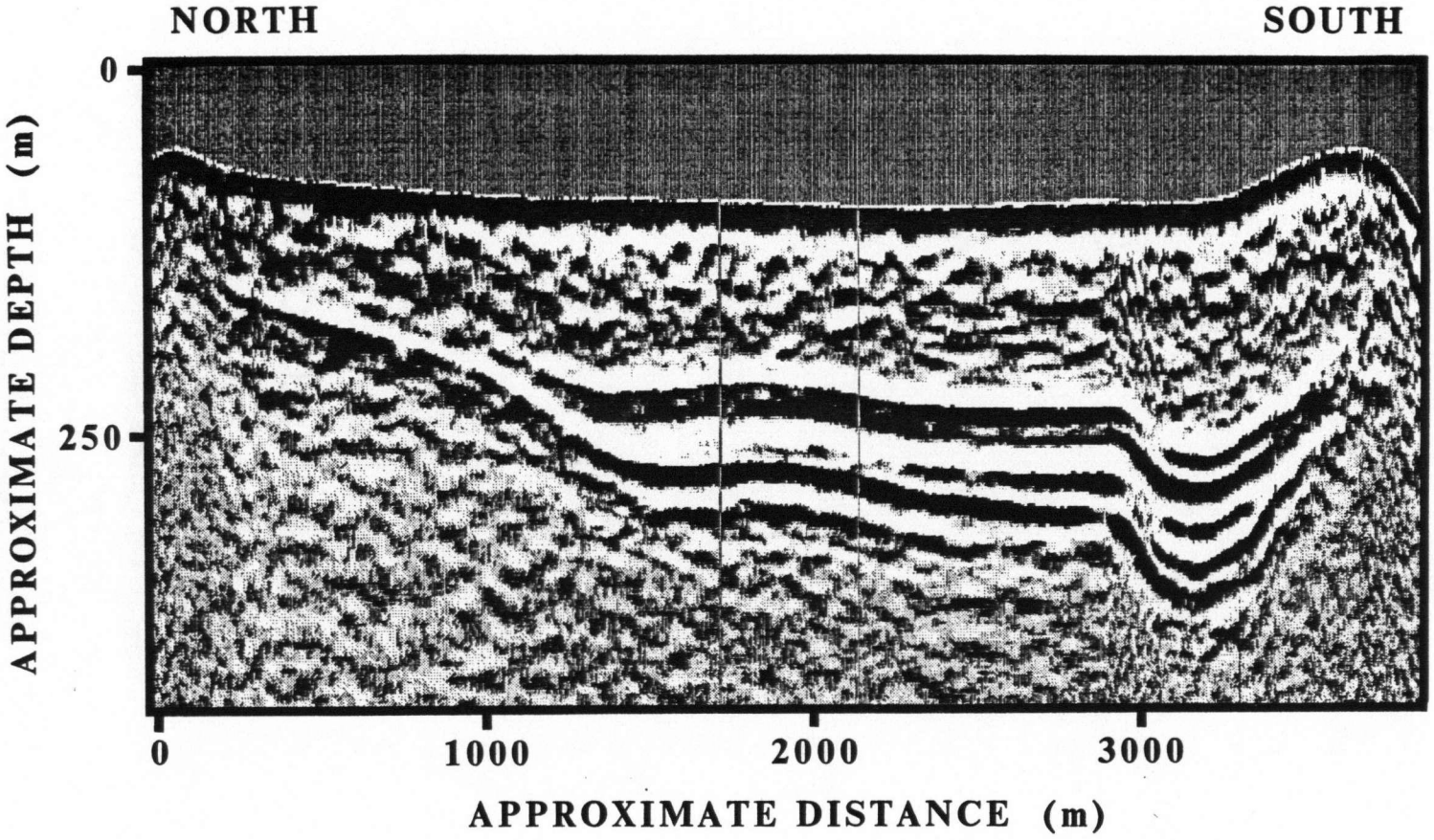

Figure 4.3. Spatially corrected depth section recorded over traverse B1. A pronounced down-warping of the radio-stratigraphy is evident near the southern end of the traverse.

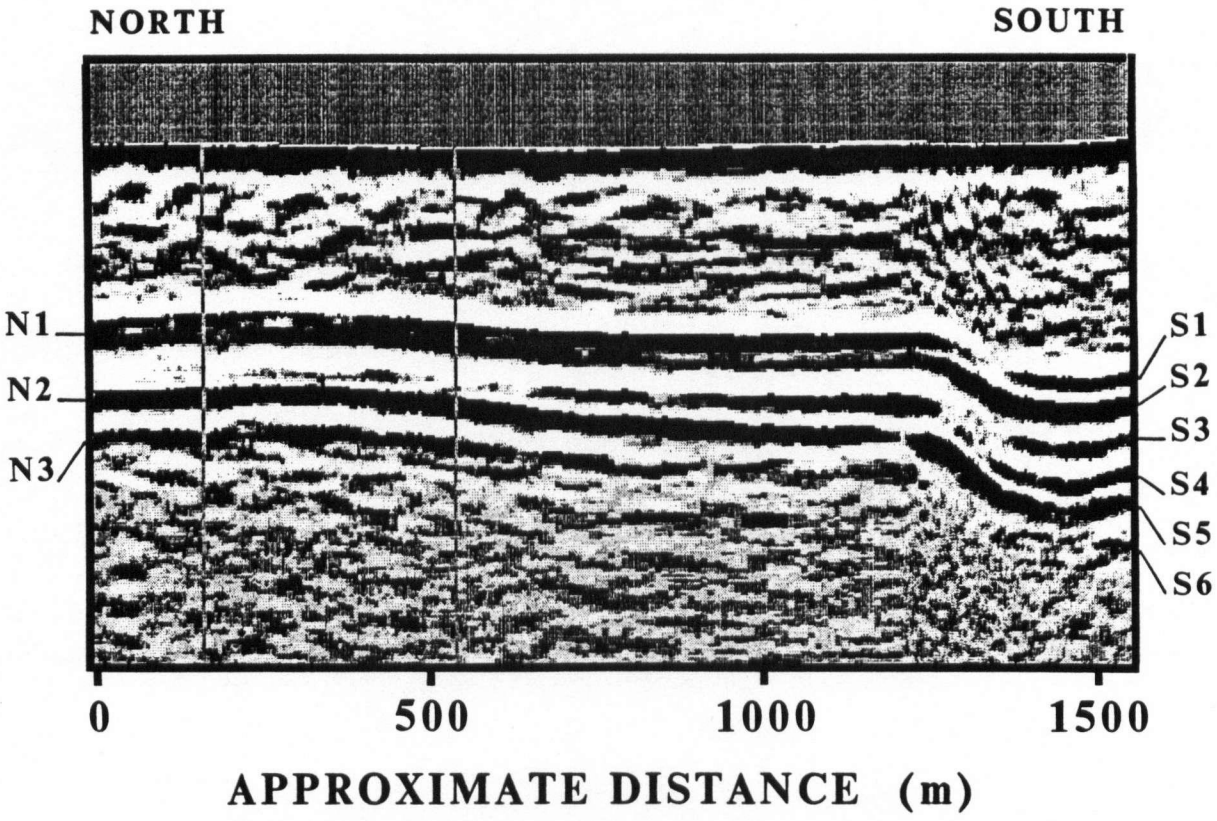

Figure 4.4. Selected interval from depth section recorded over traverse B1, depicting stratigraphic evidence for composite reflections at depth. N1, N2 and N3 denote a sequence of relatively continuous reflecting horizons, as detected within the central region of the caldera. Gradual thickening of depositional layers toward the southern rim produces dramatic variations in the recorded interference pattern. The same stratigraphic section that gives rise to N1, N2 and N3, produces a stratified sequence of apparent layers, S1, S2, S3, S4, S5 and S6, at the southern extreme of the interval. The transition involves appearance, disappearance, separation and coalescence of apparent layers.

lateral spreading and basal melting. From conservation of mass under steady-state conditions, $\partial\rho/\partial t = 0$, we obtain

$$w\frac{d\rho}{dz} + \rho\dot{\epsilon}_{kk} = 0, \tag{4.16}$$

where w represents the surface normal component of flow velocity, ρ denotes depth stratified density and $\dot{\epsilon}_{kk} = \partial V_k/\partial X_k = \Delta + dw/dz$ is the normal strain rate. The horizontal flow divergence, $\Delta = \partial u/\partial x + \partial v/\partial y$, is determined at the surface, Δ_o, from ice motion measurements. It is assumed that the two-dimensional divergence remains constant to a stagnation depth, z_s, roughly corresponding to ice thickness at the head of Long Glacier. At depths exceeding the stagnation depth, lateral divergence is assumed negligible. The depth rate of change in surface normal transport velocity is, thus, given by

$$\frac{dw}{dz} = \frac{w}{\rho}\frac{d\rho}{dz} - \Delta, \tag{4.17}$$

where

$$\Delta = \begin{cases} \Delta_o, & 0 \leq z \leq z_s \\ 0, & z > z_s \end{cases}.$$

The coupled differential equation describing depth dependent densification was presented in section 2.4.1 (Equation 2.12). Depositional age, t_a, as a function of surface normal depth, follows by integrating

$$\frac{dt_a}{dz} = \frac{1}{w}. \tag{4.18}$$

Physical parameters influencing the resulting depositional age distribution include: glacier thickness, horizontal surface flow divergence and rates of surface accumulation and basal melting. Critical sensitivity to the surface flow divergence requires a well controlled estimate obtained by numerical analysis of ice motion measurements.

4.4.2 Analysis of Horizontal Surface Flow Divergence

Precise motion surveys were conducted at the surface of the caldera glacier in 1965-66 and 1975-76 (Appendix 1). We describe the distribution of surface flow velocity in terms of third degree polynomial distributions:

$$V_x(x,y) = c_{x1} + c_{x2}x + c_{x3}y + c_{x4}xy + c_{x5}x^2 + c_{x6}y^2 + c_{x7}x^2y + c_{x8}xy^2 + c_{x9}x^3 + c_{x10}y^3 \quad (4.19)$$

and

$$V_y(x,y) = c_{y1} + c_{y2}x + c_{y3}y + c_{y4}xy + c_{y5}x^2 + c_{y6}y^2 + c_{y7}x^2y + c_{y8}xy^2 + c_{y9}x^3 + c_{y10}y^3. \quad 4.20)$$

Coefficients are determined by fitting the polynomial surfaces to localized measurements of horizontal velocity components, V_x and V_y, subject to minimization of squared error. A second degree polynomial describing horizontal surface flow divergence follows

as

$$\begin{aligned}\Delta_o(x,y) &= \frac{\partial V_x}{\partial x} + \frac{\partial V_y}{\partial y} \\ &= (c_{x2} + c_{y3}) + (2c_{x5} + c_{y4})x + (c_{x4} + 2c_{y6})y \\ &+ 2(c_{x7} + c_{y8})xy + (3c_{x9} + c_{y7})x^2 + (c_{x8} + 3c_{y10})y^2. \qquad (4.21)\end{aligned}$$

In the vicinity of Long Glacier, resulting distributions (Figure 4.5) indicate a rapid increase in both flow rate and divergence. While such a trend is expected, the "fit" is not well constrained within that region and predicted values are highly suspect. Efforts to derive a speculative volcanic record are therefore directed to the central region of the caldera, where the horizontal surface flow divergence is most highly constrained and, thus, most reliable. Note that, with the exception of a single motion stake, durations over which flow velocities are determined do not exceed 83 days. Consequently, estimation of the flow divergence is completely insensitive to long term variations caused by climatic fluctuations. Unaccountable variability of this nature poses an additional source of error in the determination of depositional age and volcanic history.

4.4.3 Conclusion: A Speculative Volcanic Record

Modelling limitations and uncertainties in the radio- stratigraphy require that conclusions concerning volcanic history be speculative. With this in mind, a preliminary volcanic record is presented in Figure 4.6. We obtain this result by filtering a spatially averaged depositional age profile for suppression of events with duration less than the

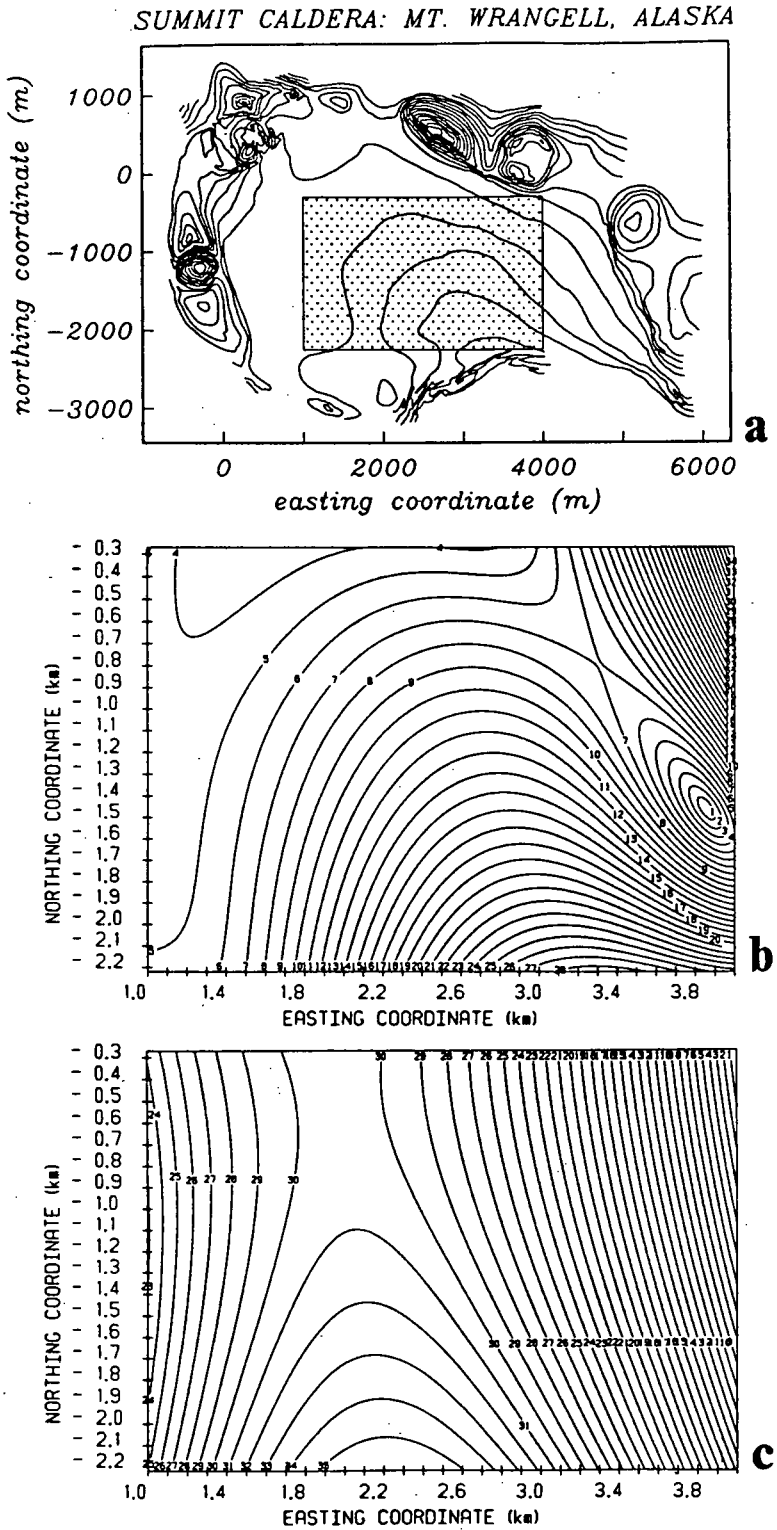

Figure 4.5. Two-dimensional distributions for surface flow rate and divergence. (a) Summit caldera map, indicating region over which the distributions are calculated. (b) Surface flow speed (range: 0.104 cm/day to 18.589 cm/day; contour interval: 0.528 cm/day). (c) Surface flow divergence (range: -4.962×10^{-2} /yr to 1.738×10^{-2} /yr; contour interval: 1.914×10^{-3} /yr).

pulse rise-time. Although the predicted sequence is found to vary significantly with locality, the record presented here is relatively well constrained. The particular profile is determined by averaging results obtained over the central region of the caldera, along traverse A1. By design, traverse A1 coincides with motion survey transect $C - C'$ (Appendix 1) so that flow dynamics are well determined.

The preliminary volcanic record extends to approximately AD 1650. If broad-scale trends in returned power are attributable to gradual periodic fluctuations in volcanic activity, the sequence suggests a periodicity of roughly 100 years. Assuming this conjecture to be plausible, a gradual increase in activity is expected at Mt. Wrangell, with a climax around AD 2025. While uncertainty in short term events is substantial, it is interesting to compare the predicted near surface record with the known eruptive history (Table 4.1). Finally, although the glacio-volcanic record preserved within the caldera is primarily attributed to fluctuations in volcanic activity at Mt. Wrangell, we do not rule out the possible influence of additional volcanic events in the Pacific northwest.

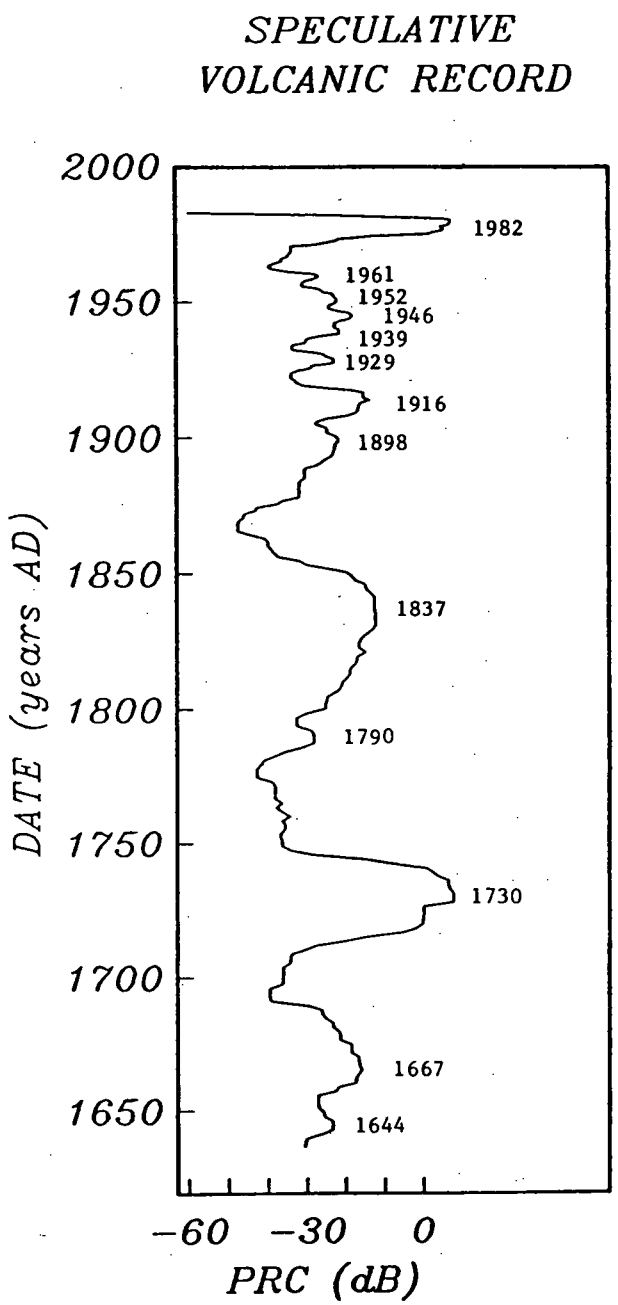

Figure 4.6. Speculative volcanic record as a function of reflected power. Positive reflection coefficients are due to approximations inherent in corrections for geometrical spreading and absorption.

EVENT	REMARKS
1930	An unspectactacular eruption from the West Crater.
1921	Most spectacular recent eruption. Probably from the northeast flank.
1912	Inferred from newspaper reports in Cordova and Valdez.
1899	Triggered by earthquake at Yakutat Bay.

Table 4.1. Known eruption record for Mt. Wrangell, Alaska.

REFERENCES CITED

Ackley, S.F., and T.E.Keliher 1979. Ice sheet internal radio- echo reflections and associated physical property changes with depth, *Journal of Geophysical Research*, **84**, 5675-5680.

Anderson, K.R., and J.E.Gaby 1983. Dynamic waveform matching, *Information Sciences*, **31**, 221-242.

Benson, C.S. 1962. Stratigraphic studies in the snow and firn of the Greenland Ice Sheet, *SIPRE Research Report* **70**, 93pp.

Benson, C.S. 1982. Glaciological-volcanological research on Mt. Wrangell, Alaska, *Final technical report on NSF grant EAR 77-15166, Geophysical Institute, University of Alaska.*

Benson, C.S., R.J.Motyka 1978. Glacier-volcano interactions on Mt. Wrangell, Alaska, *Annual Report, 1977-78, Geophysical Institute, University of Alaska*, 1-25.

Bingham, D.K. 1967. Ice motion and heat flow studies on Mt. Wrangell, Alaska, M.S. thesis, University of Alaska, 117p.

Boutron, C., and C.Lorius 1979. Trace elements in Antarctic snows since 1914, *Nature*, **277**, 551-554.

Camplin, G.C., J.W.Glen, and J.G.Paren 1978. Theroretical models for interpreting the dielectric behaviour of HF-doped ice, *Journal of Glaciology*, **21**, 123-142.

Claerbout, J.F., and F.Muir 1973. Robust modelling with erratic data, Geophysics, **35**, 826-844.

Clarke, G.K.C., and C.S.Benson 1983. An interpretation model for the glacier in the Mt. Wrangell caldera, Alaska, Internal report, Department of Geophysics and Astronomy, University of British Columbia, Vancouver, Canada, 19p.

Clarke, G.K.C., G.M.Cross, and C.S.Benson 1987. Airborne UHF radar measurements of caldera geometry and volcanic history, Mt. Wrangell, Alaska, *Annals of Glaciology*, In press.

Clough, J.W. 1977. Radio-echo sounding: reflections from internal layers in ice sheets, *Journal of Glaciology*, **18**, 3-14.

Evans, J.R. 1982. Running median filters and a general despiker, *Bulletin of the Seismological Society of America*, **72**, 331-338.

Evans, S. 1965. Dielectric properties of ice and snow: a review, *Journal of Glaciology*, **5**, 773-792.

Evans, S., and B.M.E.Smith 1969. A radio-echo equipment for depth sounding in polar ice sheets, *Journal of Scientific Instruments (Journal of Physics E)*, Series **2(2)**, 131-136.

Fitch, E.P., E.J.Coyle, and N.C.Gallagher 1984. Root properties and convergence rates of median filters, *IEEE Transactions on Acoustics, Speech and Signal Processing*, **5**, 739-746.

Gudmandsen, P. 1975. Layer echoes in polar ice sheets, *Journal of Glaciology*, **15**, 95-101.

Hammer, C.U. 1977. Past volcanism revealed by Greenland Ice Sheet impuities, *Nature*, **270**, 482-486.

Hammer, C.U. 1980. Acidity of polar ice cores in relation to absolute dating, pat volcanism, and radio-echoes, *Journal of Glaciology*, **25**, 359-372.

Hammer, C.U., H.B.Clausen, and W.Dansgaard 1980. Greenland Ice Sheet evidence of post-glacial volcanism and its climatic impact, *Nature*, **288**, 230-235.

Hammer, C.U., H.B.Clausen, W.Dansgaard, N.Gundestrup, S.J.Johnsen, and N.Reeh 1978. Dating Greenland ice cores by flow models, isotopes, volcanic debris, and continental dust, *Journal of Glaciology*, **20**, 3-26.

Harrison, C.H. 1971. Radio-echo sounding: focussing effects in wavy strata, *Geophysical Journal of the Royal Astronomical Society*, **24**, 383-400.

Harrison, C.H. 1972. Radio propagation effects in glaciers, Ph.D. thesis, University of Cambridge, 193p.

Harrison, C.H. 1973. Radio-echo sounding of horizontal layers in ice, *Journal of Glaciology*, **12**, 383-397.

MacKeith P., Unpublished field notes for 1976-1978 seasons at Mt. Wrangell, 1978.

Motyka, R.J. 1983. Volcanological research on Mt. Wrangell caldera, Alaska utilizing the natural glacier ice as a calorimeter, Ph.D. thesis, University of Alaska.

Motyka, R.J., P.MacKeith, and C.S.Benson 1980. Mt. Wrangell: utilization of glacier ice to measure heat flow and infer thermal regime, *EOS*, **61**, 66.

Millar, D.H.M. 1981a. Radio-echo layering in polar ice sheets, Ph.D. thesis, University of Cambridge, 177p.

Millar, D.H.M. 1981b. Radio-echo layering in polar ice sheets and past volcanic activity, *Nature*, **292**, 441-443.

Millar, D.H.M. 1982. Acidity layers in ice sheets from radio-echo sounding, *Annals of Glaciology*, **3**, 199-203.

Myers, C.S., and L.R.Rabiner 1981. A comparative study of several dynamic time-warping algoritms for connected-word recognition, *Bell System Technology Journal*, **60**, 1389-1409.

Narod, B.B., and G.K.C.Clarke 1980. Airborne UHF radio-echo sounding of three Yukon glaciers, *Journal of Glaciology*, **25**, 23-31.

Narod, B.B., and G.K.C.Clarke 1983. UHF radar system for airborne ice thickness surveys, *Canadian Journal of Earth Sciences*, **20**, 1073-1086.

Neal, C.S. 1976. Radio-echo power profiling, *Journal of Glaciology*, **17**, 527-530.

Neal, C.S. 1977. Radio-echo studies of the Ross Ice Shelf, Ph.D. thesis, University of Cambridge.

Neidell, N.S., and M.T.Taner 1971. Semblance and other coherency measures for multichannel data, *Geophysics*, **36**, 482-497.

Nodes, T.A., and N.C.Gallagher 1982. Median filters: some modifications and their properties, *IEEE Transactions on Acoustics, Speech and Signal Processing*, **5**, 739-746.

Oswald, G.K.A. 1975. Radio-echo sounding of polar glacier beds, Ph.D. thesis, University of Cambridge, 134p.

Paren, J.G. 1970. Dielectric properties of ice, Ph.D. thesis, University of Cambridge.

Paren, J.G. 1981. Reflection coefficient at a dielectric interface, correspondence, *Journal of Glaciology*, **27**, 203-204.

Paren, J.G., and G.de Q.Robin 1975. Internal reflections in polar ice sheets, *Journal of Glaciology*, **14**, 251-259.

Prager, B.T. 1993. Digital signal procesing of UHF radio-echo sounding data from Ellesmere Island, M.Sc. thesis, University of British Columbia, 88p.

Press, F., and R.Siever 1974. *Earth*, W. H. Freeman and Company, San Francisco, U.S.A., 945p.

Robin, G.de Q., S.Evans, and J.T.Bailey 1969. Interpretation of radio-echo sounding in polar ice sheets, *Philosophical Transactions of the Royal Society, Series A*, **265**, 437-505.

Robinson, J.C. 1970. Statistically optimal stacking of seismic data, *Geophysics*, **35**, 436-446.

Sheriff, R.E., and L.P.Geldhart 1983. *Exploration Seismology: Data Processing and Interpretation*, Cambridge University Press, Cambridge, U.K., 221p.

Smith, B.M.E. 1971. Radio-echo studies of glaciers, Ph.D. thesis, University of Cambridge, 157p.

Smith, B.M.E., and S.Evans 1972. Radio-echo sounding: absorption and scattering by water inclusions and ice lenses, *Journal of Glaciology*, **11**, 133-146.

Walford, M.E.R. 1968. Field measurements of dielectric absorption in antarctic ice and snow at very high frequencies, *Journal of Glaciology*, **7**, 89-94.

Westphal, J.A. 1963. Personal communication in Evans, 1965.

Whillans, I.M. 1976. Radio-echo layers and the recent stability of the West Antarctic Ice Sheet, *Nature*, **264**, 152-155.

GENERAL REFERENCES

Bogordsky, V.V., C.R.Bentley, and P.E.Gudmandsen 1985. *Radioglaciology*, D. Reidel Publishing Company, Dordrecht, Holland, 254p.

Paterson, W.S.B. 1981. *The Physics of Glaciers*, Pergamon Press, Oxford, U.K., 380p.

Skolnik, M.I. 1962. *Introduction to Radar Systems*, McGraw- Hill Book Company, New York, U.S.A., 648p.

APPENDIX

GLACIER MOTION MEASUREMENTS

Figures A.1 and A.2 illustrate stake positions surveyed for ice motion measurements in 1965-66 (Bingham, 1967) and 1975-76 (Motyka, 1983) respectively. Corresponding data utilized for the present analysis of horizontal surface flow divergence are tabulated in Tables A.1 and A.2.

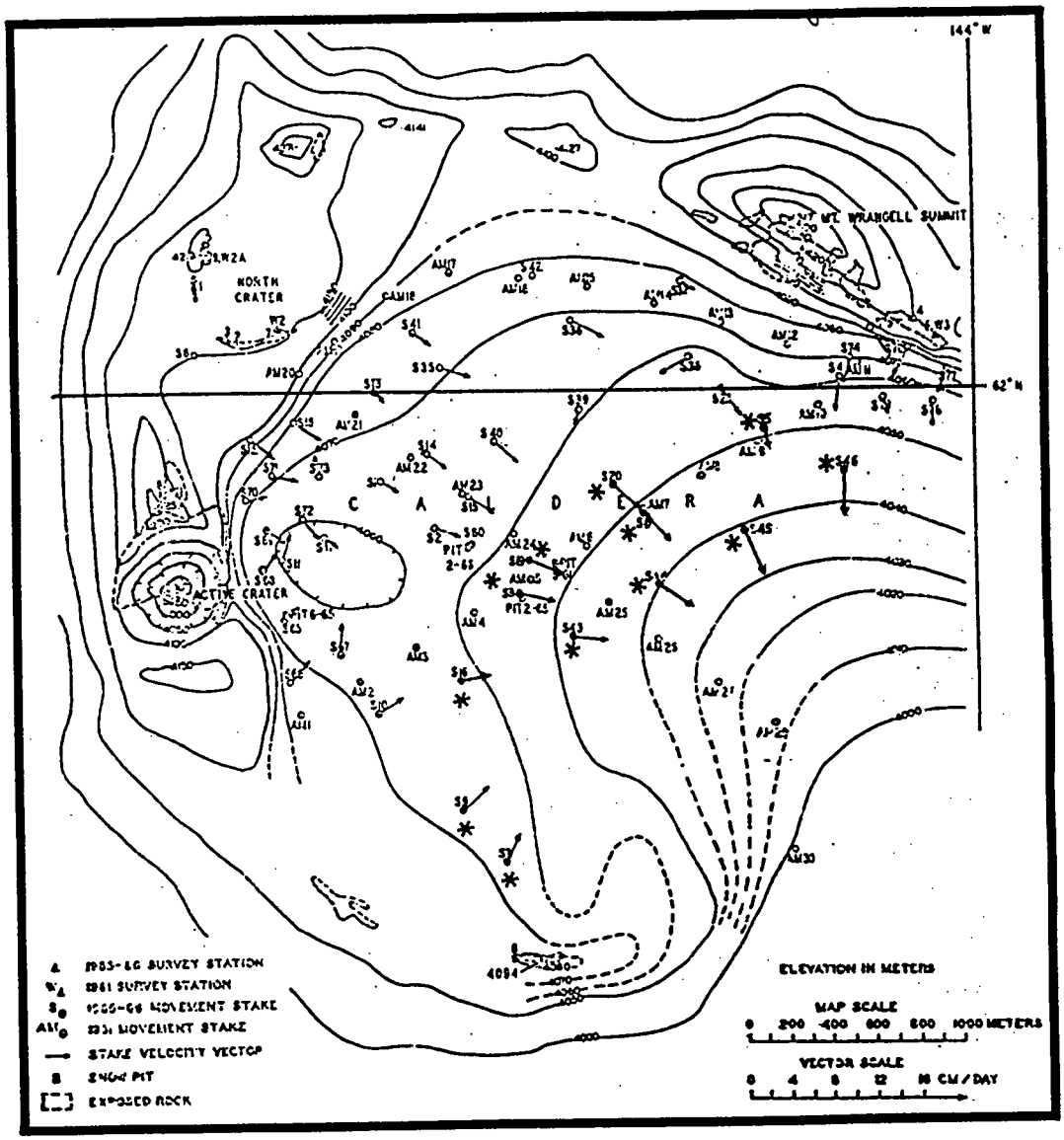

Figure A.1. Map of the summit caldera, depicting original location and horizontal velocity vectors for ice motion stakes surveyed over 1965-66 (from Bingham, 1967).

STAKE	EASTING (m)	NORTHING (m)	INTERVAL (days)
S3	1322.47	-1207.24	
	1322.39	-1207.72	56.15
S5	2485.58	-434.72	
	2485.91	-436.40	56.13
S6	1911.51	-823.54	
	1913.06	-825.12	56.13
S7	1236.02	-2499.05	
	1236.38	-2498.26	27.58
S9	1038.03	-2249.52	
	1039.40	-2248.28	56.15
S16	1037.47	-1618.17	
	1039.01	-1617.91	56.13
S19	1367.99	-1041.48	
	1369.70	-1042.26	56.13
S20	1771.40	-692.40	
	1772.90	-693.81	56.13
S43	1574.26	-1411.84	
	1575.10	-1411.95	23.58
S44	1979.83	-1166.60	
	1980.61	-1167.13	23.58
S45	2399.31	-912.32	
	2399.69	-913.35	23.58
S46	2853.10	-637.20	
	2853.07	-638.25	23.58

Table A.1. Horizontal motion components; 1965-66 survey (from Bingham, 1967).

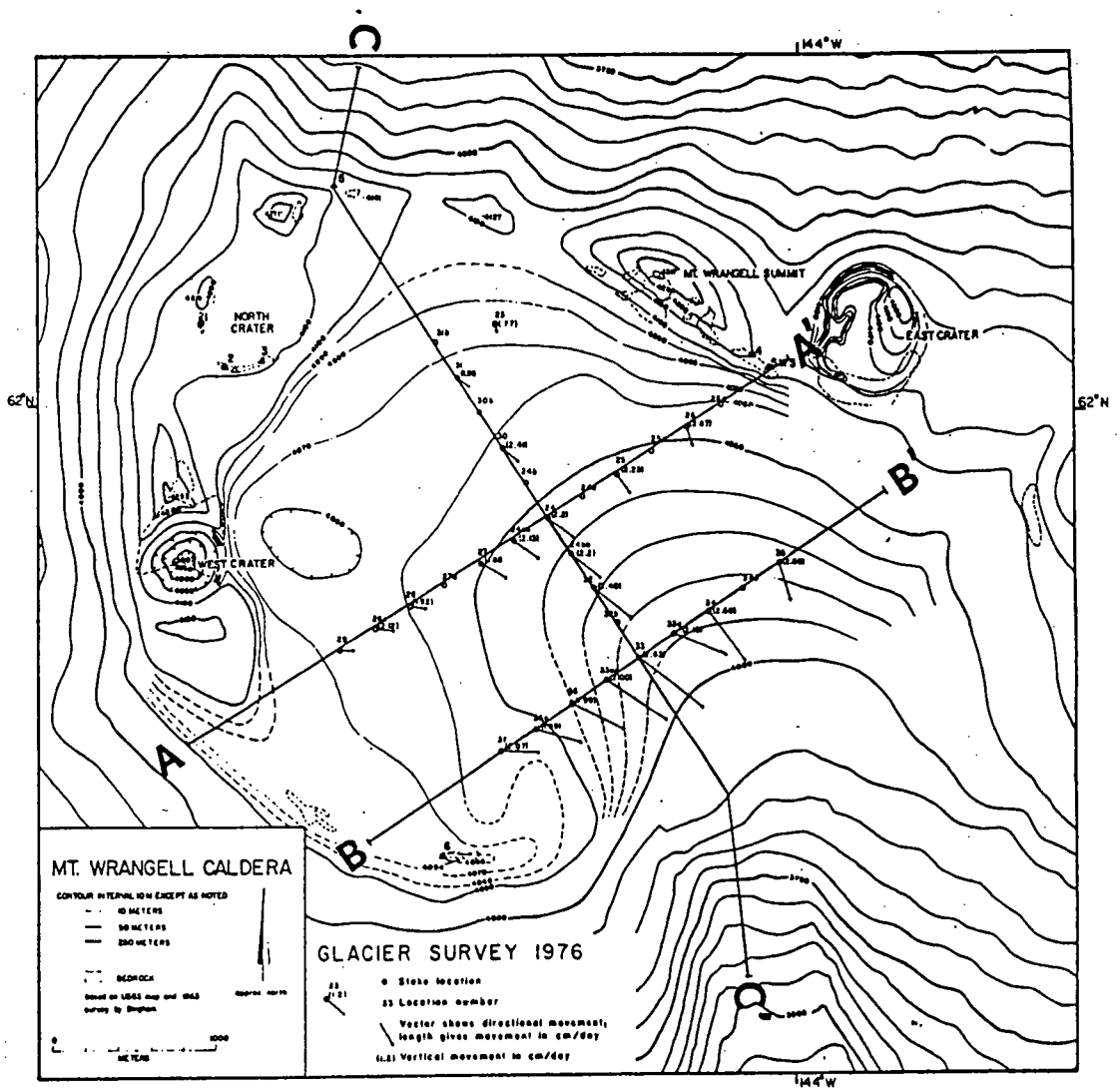

Figure A.2. Map of the summit caldera, depicting original location and horizontal velocity vectors for ice motion stakes surveyed over 1975-76 (from Motyka, 1983).

STAKE	EASTING (m)	NORTHING (m)	INTERVAL (days)
23	1592.25	266.95	
	1592.71	264.43	307.0
24	1909.11	-896.43	
	1911.34	-898.12	71.5
24aa	1696.84	-1030.71	
	1699.04	-1032.29	71.5
24bb	2046.99	-1107.67	
	2049.58	-1109.77	71.5
25	2333.09	-629.14	
	2334.28	-630.80	71.5
26	2760.73	-359.79	
	2761.24	-361.32	71.5
27	1483.63	-1163.97	
	1485.94	-1165.28	71.5
28	1059.63	-1431.80	
	1060.98	-1431.59	71.5
28a	846.19	-1565.89	
	847.87	-1565.73	71.5
29	633.21	-1699.71	
	634.52	-1699.68	71.5
30	1633.96	-475.57	
	1635.28	-475.67	71.5
31	1358.78	-56.26	
	1359.99	-57.17	71.5
32	2185.75	-1320.26	
	2188.93	-1322.96	71.5
33	2463.37	-1745.85	
	2468.95	-1750.36	71.5
33aa	2252.93	-1885.48	
	2258.45	-1889.18	73.0
34	2884.00	-1465.74	
	2887.36	-1470.17	73.0
35	3307.68	-1184.14	
	3308.72	-1187.47	73.0

* (continued on following page)

STAKE	EASTING (m)	NORTHING (m)	INTERVAL (days)
36	2042.99	-2024.97	
	2047.73	-2027.25	83.0
36a	1831.60	-2165.08	
	1835.71	-2166.38	83.0
37	1619.22	-2306.82	
	1622.65	-2306.70	83.0

Table A.2. Horizotal motion components; 1975-76 survey (from Motyka, 1983).